University of Alberta

The Kubo conductivity tensor for 2- and 3-dimensional magnetic nulls

by

Denis A. St-Onge

A thesis submitted to the Faculty of Graduate Studies and Research in partial fulfillment of the requirements for the degree of

Master of Science

Department of Physics

Spring 2011
Edmonton, Alberta

Examining Committee

Dr. Richard Sydora, Physics

Dr. Carsten Krauss, Physics

Dr. Robert Fedosejevs, Electrical and Computer Engineering

Abstract

The complete set of Kubo conductivity tensors are computed in two- and three-dimensional linear magnetic null systems using collisionless single-particle simulations. Chaos regions are constructed for each case, along with the complete Lyapunov spectrum. It is found that stochastic frequency mixing of particle bounce motion, as well as gyromotion, contribute significantly to the conductivity. For many cases, the conductivity curve is well approximated by power-laws, resulting in a divergent value of the direct-current conductivity, while others can be described by a sum of Maxwellian curves. The energy dissipation of these systems is also briefly discussed.

Acknowledgements

I would like to thank my supervisor Dr. Richard Sydora for giving me the opportunity to work on such an interesting project, as well as guiding me through all the hardships that came along the way.

I would also like to thank the people at Academic Information and Communication Technologies, as well as the people at various Westgrid clusters, for providing me the computational resources needed in order to perform this study.

Finally, this research was supported by a PSG-M award granted by the Natural Sciences and Engineering Research Council of Canada.

Table of Contents

List of Tables

List of Figures

Chapter 1

Introduction

Magnetic reconnection is the process in which magnetic field lines from two or more distinct fields re-assemble themselves in a plasma to form new magnetic configurations. This is driven by the release of stored magnetic energy through dissipative processes such as classical collisions or anomalous resistivity. The consequence of reconnecting magnetic fields is a magnetic null (alternatively a magnetic neutral point) which is the area between distinct magnetic domains, providing the magnitude of the field becomes zero.

Historically, magnetic nulls have played an important role in magnetic reconnection as far back as 1947 when Giovanelli [4] suggested that an electric field near a magnetic null point could have the ability to accelerate free electrons, leading to a possible mechanism for solar flares. Neutral points were soon applied to models of the magnetosphere in 1949 by Hoyle [5]. It was Dungey [6] in 1953 who developed the theory of magnetic reconnection and its relation to magnetic neutral points. Electric fields near null points can heat and accelerate particles towards areas of stronger magnetic field, resulting in energy being carried away from the magnetic field which drives magnetic reconnection. Other various types of phenomena, from space plasmas to laboratory plasmas, have also been attributed to magnetic reconnection. Recently, the European Space Agency Cluster observed a three-dimensional magnetic null

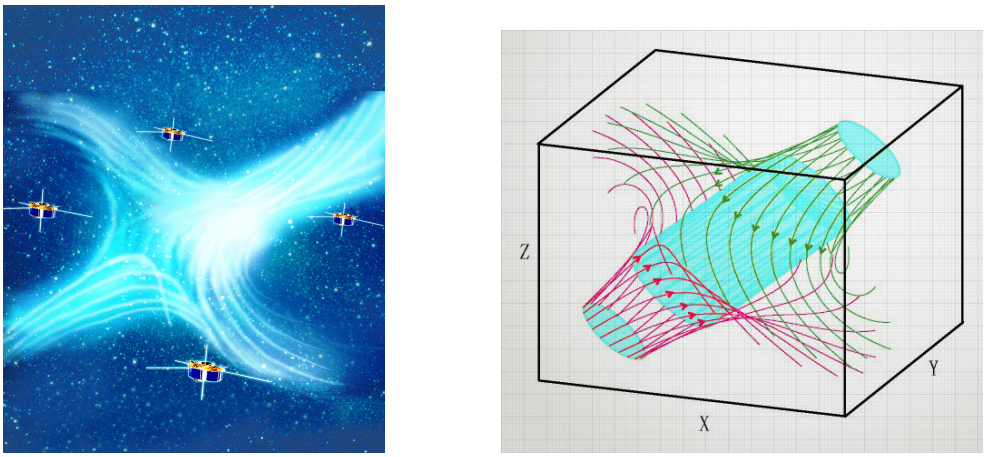

(a) (b)

Figure 1.1: (a) Artist's impression of the magnetic null found by the four ESA Cluster spacecraft. (b) Sketch of the same magnetic null shows a three-dimensional spiral structure. Source: [1]

in the earth's magnetosphere [7, 1]. Fig. 1.1 (a) shows an artist's impression of this null, while Fig. 1.1(b) shows the underlying three-dimensional structure. Stark *et al.* [8] probed the ion velocity distribution function by using laser-induced fluorescence during a reconnection event, finding that the heating of the ions was proportional to the amplitude of the reconnection drive. Reconnection can also be an important mechanism in tokamaks. Fitzpatrick and Hender [9] showed that, providing an electrical perturbation is driven near a natural mode frequency, reconnection can occur. Fitzpatrick later showed [10] that a strong enough perturbation can also drive reconnection even when the perturbation frequency is far removed from a natural mode frequency.

The major limitation to magnetic reconnection is in the calculation of the time and length scale of the process. While collisional reconnection processes can be modeled fairly well over uniform resistivities, systems with non-uniform resistivities, as well as three-dimensional reconnection, are less understood. The theory behind collisionless reconnection is also not very well-developed. The time scale of an average solar flare is of the order of $10^2 - 10^3$ seconds. Slow

reconnection models have been developed by Sweet [11] and Parker [12]. Parker calculated a time scale of 5×10^4 seconds, which is much too large to account for solar flares. However, Parker's choice of scale has been criticized by Axford and Yeh [13], which should be determined by the boundary conditions of the flow. A fast reconnection mechanism was formulated by Petschek [14] and has been generalized a number of times [15, 16]. While this mechanism yields correct time scales, in the past MHD simulations have failed to reproduce these results when applied to nulls with homogeneous resistivity [17]. Recently, Baty *et al.* have been able to reproduce correct time scales using Petschek reconnection over homogeneous resistivity by using non-uniform viscosity profiles [18].

One important aspect of magnetic reconnection is the conductivity (or resistivity) around the point of reconnection, where the magnitude of the conductivity can determine the time-scale of the reconnection by calculating the dissipation D

$$D = \int_S \mathbf{E}\cdot\mathbf{j}dx, \tag{1.1}$$

where $\mathbf{E}$ is the electric field, $\mathbf{j}$ is the current, and S is the boundary of the dissipation region. To determine $\mathbf{E}$, Ohm's law can be used for low-β magnetic fields,

$$\mathbf{j} = \sigma\mathbf{E}, \tag{1.2}$$

where σ is the conductivity tensor. In general, for classical systems, σ is symmetric provided that the sign of the magnetic field is changed, i.e. $\sigma_{ab}(\mathbf{B}) = \sigma_{ba}(-\mathbf{B})$, which is a result of the Onsager reciprocity relations [19]. The conductivity tensor can be formulated to be dependent on the frequency of the applied electric field. $\sigma(\omega = 0)$ is known as the direct current (DC) value of the conductivity tensor, while $\sigma(\omega \neq 0)$ is known as the alternating current (AC) conductivity tensor. There is no exact method of calculating the conductivity tensor, therefore many methods must be studied and compared, with smaller

conductivities being more important than larger ones. The conductivity was classically calculated based on the collision frequency of particles with one another. This inverse conductivity is called the Spitzer resistivity [20] and has the form

$$\eta \approx \frac{\pi q_s^2 m_s^{1/2}}{(4\pi\epsilon_0)^2 (k_\mathrm{B} T_s)^{3/2}} \ln \Lambda \tag{1.3}$$

where m_s, q_s and T_s is the particle mass, charge, and temperature of species s, respectively, k_B is the Boltzmann constant and the Coulomb logarithm Λ is defined as

$$\Lambda = \frac{\lambda_\mathrm{D}}{r_0}. \tag{1.4}$$

Here, λ_D is the ion skin depth and r_0 is the maximum impact parameter. Typically, $\Lambda \sim 10$ in laboratory plasmas, $\Lambda \sim 20$ in solar coronas, and $\Lambda \sim 30$ in the magnetosphere [21]. It is important to consider the fact that the observable quantity for most cosmic systems is the current, not the electric field. From this is it helpful to use the resistive form of Ohm's law

$$\mathbf{E} = \rho \mathbf{j} \tag{1.5}$$

where ρ is the resistivity tensor. It is easy to see that ρ is the matrix inverse of σ. For a conductivity tensor with no off-diagonal components, $\sigma_{aa} = \rho_{aa}^{-1}$. However, this does not hold for tensors with off-diagonal components.

In 1969, Speiser showed that resistivity can exist without particle collisions or wave interactions [22]. He derived two collisionless resistivities, one based on the gyromotion of particles and one based on non-adiabatic acceleration around regions of diffusion. Another method for calculating the conductivity is by using the Kubo formula [23], which is based on applying the fluctuation-dissipation theorem [24] to electromagnetic fields. The method uses the ensemble averaged correlation function of the velocities to compute the conductivity. One advantage of the Kubo conductivity is its ability to compute conductivities over an entire spectrum of applied electric fields. Similar to the Kubo

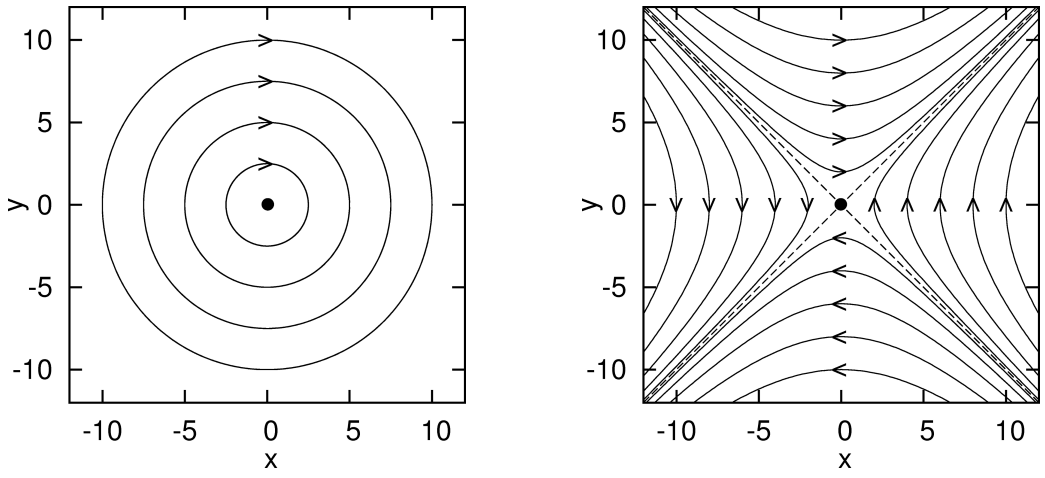

Figure 1.2: Examples of two-dimensional O-type (a) and X-type (b) null points. The O-type null has the magnetic field $\mathbf{B} = b_0\,(y, -x, 0)$ while the X-type null has the magnetic field $\mathbf{B} = b_0\,(y, x, 0)$. Lines represent magnetic field lines, while dashed lines signify the separatrix in the X-type null cases. The null point is denoted by a dot at the origin. All units are reduced.

conductivity is the linearized Vlasov conductivity, which is derived by using a kinetic theory of plasmas. For ergodic systems, the Kubo conductivity and linearized Vlasov conductivity are equivalent [25].

Until the early 90s, research was mainly focused on the study of two-dimensional linear magnetic nulls. As the region of interest is usually very close to the null point, many two-dimensional magnetic systems can be expanded into a linear system which is topologically and computationally simpler to work with. The two main types of 2D linear nulls are O-point nulls and X-point nulls, as shown in Fig. 1.2. The magnetic O-point is a location of zero magnetic field surrounded by connected magnetic field lines. An example of this would be a null point surrounded by concentric circular magnetic field lines. A magnetic X-point has four distinct magnetic field domains separated by an X-shaped separatrix where the intersection is a point with no magnetic field. As the O-type magnetic null deals with a single magnetic domain, its application to magnetic reconnection is limited. Most focus has been on

the study of the X-type magnetic null point. Martin [26] studied the chaotic dynamics of the two-dimensional X-point using the method of Lyapunov exponents for a variety of situations. It was found that even without an applied electric field, dynamics around a null point are generally chaotic. Numata and Yoshida [2] calculated the conductivity of an expanded X-point (known as a double Y-point) by using a conductivity similar to that derived by Speiser and calculated the reconnection dynamics by using Petschek's model. It was found that a single chaos zone, while enhancing the resistivity of the system, cannot solely account for fast-type reconnection.

Horton *et al.* studied the collisionless DC conductivity in a two-dimensional approximation to the magnetic null in the geomagnetic tail by using the Vlasov conductivity in a series of papers [27, 28, 25]. It was found that stochastic processes near the magnetic null resulted in power-law decays of the correlation of velocities, with an effective collision time, proportional to the cyclotron period, being used to calculate the energy dissipation of the system. Holland and Chen [29] criticized the use of the Vlasov conductivity in a number of ways, where they stated that the use of the Vlasov conductivity may not satisfy the necessary conditions needed to render it valid near magnetic null points. It was also found that the Vlasov conductivity was sensitive to the total integration time of the simulation. For long simulation times, particles would also spent most of the simulation in non-chaotic regions, rendering a definition of conductivity based on chaotic motion ambiguous. Afterwards, they proposed a method to find the energy dissipation of particles based on a method by Cowley [30], which is derived from the difference of ingoing and outgoing particle pitch angles. Finally, they note that their results contradict results found by Speiser [22], stating that the simple relation $\mathbf{j} = \sigma\mathbf{E}$ may not be valid in plasmas. Hernandez *et al.* published a counter-rebuttal [31], stating that long-term correlated motion near regions of chaos lead to impor-

tant contributions to the conductivity calculation, as well as arguing that the necessary conditions are met in order to apply the Vlasov conductivity.

In recent years, more attention has been given to the reconnection near three-dimensional null points. These null points offer a large variety of different topological configurations. Cowley [32] first studied the structure of a three-dimensional potential null with form $\mathbf{B} = (\alpha x, \beta y, -(\alpha + \beta)z)$, stating that the neutral point consisted of a spine with field-lines expanding to a so-called fan plane. Fukao [33] studied more general neutral points, finding spiral structures. He noted that in general, the spine and the fan of the null are not perpendicular. Parnell *et al.* performed a complete study on all possible types of three-dimensional linear nulls, as well as degenerate two-dimensional null cases [3].

Priest and Titov [34] studied the reconnection of a number of three-dimensional null points, finding two types of reconnection (denoted as fan reconnection and spine reconnection) unique to both the fan plane and the spine. It was also found that reconnection and consistent electric field are strongly dependent on the boundary conditions around the null point. The reconnection between two adjacent three-dimensional null points was also briefly mentioned. Parnell *et al.* have also shown that X-ray bright points in solar flares are the result of reconnection near three-dimensional null points [35]. Priest, in a recent paper [36], has reclassified the types of three-dimensional reconnection by now using three separate categories, called torsional spine reconnection, torsional fan reconnection, and spine-fan reconnection.

Recently, Priest and Forbes [37] have shown that magnetic reconnection can occur even in the absence of magnetic nulls. One such process where this occurs is magnetic flipping, where large gradients in the magnetic field cause greatly accelerated currents. These currents, in a resistive MHD model, drive field line velocity. If this velocity is greater than the Alfvén velocity, magnetic

field lines can experience dissipation and "flip" into different domains.

The purpose of this study is to construct the complete frequency-dependent conductivity tensor of every case listed in Parnell's study [3] by using the Kubo conductivity formula. The conductivity of the system in Numata [2] will also be computed from the Kubo conductivity in order to give a comparison between Kubo's conductivity and Speiser's conductivity. Lyapunov exponents for all systems shall be computed to better understand the underlying chaotic dynamics. Finally, the energy dissipation will be computed and compared to regular dynamics further away from magnetic null points.

This thesis is organized into the following sections: Sec. 2 explains the theory behind Lyapunov exponents and the conductivities of interest, as well as explaining the underlying mechanics of the computer simulations. Sec. 3 deals with the study of the two-dimensional system from Numata [2], as well as the comparison of the Kubo and Speiser conductivities. Sec. 4 contains the study of the three-dimensional null systems outlined in Parnell [3], as well as a discussion of the results. The summary of this thesis is presented in Sec. 5 along with possible extensions of this research.

Chapter 2

Methodology

2.1 Numerical Approach

The simulation of microscopic particle dynamics in the vicinity of magnetic nulls is based on a system of non-interacting particles in an electromagnetic field with the equations of motion

$$m\frac{d\mathbf{u}}{dt} = q(\mathbf{E}(\mathbf{x}) + \mathbf{u} \times \mathbf{B}(\mathbf{x})), \tag{2.1}$$

where q and m are the charge and mass of the particle, respectively. In this simulation normalized units are used where $\hat{\mathbf{x}} = \mathbf{x}/l_x$, $\hat{\mathbf{b}} = \mathbf{B}/B_o$, $\hat{t} = t/\tau_\mathrm{A}$, $\hat{\mathbf{u}} = \mathbf{u}/v_\mathrm{A}$, $\hat{\mathbf{e}} = \mathbf{E}/m_\mathrm{A}v_\mathrm{A}B_o$, where v_A is the Alfvén velocity, B_0 is the magnitude of the magnetic field, $\tau_\mathrm{A} \equiv l_x/v_\mathrm{A}$, l_x is the scale-length of the experiment, and m_A is the Alfvén mach number. The magnetic field in the Alfvén velocity is taken as the unit magnetic field (i.e. where $\hat{\mathbf{x}} = (1, 0, 0)$). This gives a normalized equation of motion

$$\frac{\lambda_i}{l_x}\frac{d\hat{\mathbf{u}}}{d\hat{t}} = m_\mathrm{A}\hat{\mathbf{e}} + \hat{\mathbf{u}} \times \hat{\mathbf{b}},$$

where $\lambda_i = c/\omega_p$. Here, c is the speed of light and ω_p is the plasma frequency for the specified particle species. For simplicity, $l_x = \lambda_i$. Although the results of this study can be scaled for both electrons and ions, it is assumed that since the ion Larmor radius is much greater than that of the electron, most effects will be the result from ion motion, as it will experience greater chaotic effects

by being closer to the magnetic null.

For a discrete-time simulation, the equations of motion are integrated implicitly with particle velocities and positions being evaluated at every integer step and the electromagnetic fields being evaluated at every half-integer step. The finite-difference equations of motion are

$$\frac{\mathbf{u}_1 - \mathbf{u}_0}{\delta t} = \frac{q}{m}\left(\mathbf{E}(\mathbf{x}_{1/2}) + \frac{\mathbf{u}_1 + \mathbf{u}_0}{2} \times \mathbf{B}(\mathbf{x}_{1/2})\right)$$
$$\frac{\mathbf{x}_1 - \mathbf{x}_0}{\delta t} = \frac{\mathbf{u}_1 + \mathbf{u}_0}{2},$$

where $\mathbf{x}_{1/2} = (\mathbf{x}_1 + \mathbf{x}_0)/2$. The two equations of motion are coupled in both $\mathbf{u}_1$ and $\mathbf{x}_1$. Assuming the change in parallel velocity is small, $\mathbf{u}_1$ can be solved as

$$\frac{\mathbf{u}_1 + \mathbf{u}_0}{2} = \frac{\mathbf{u}_0 + \mathbf{u}_0 \times \left(\frac{q\delta t \mathbf{B}_{1/2}}{2m}\right) + \mathbf{u}_0 \cdot \left(\frac{q\delta t \mathbf{B}_{1/2}}{2m}\right)\left(\frac{q\delta t \mathbf{B}_{1/2}}{2m}\right)}{1 + \left(\frac{q\delta t \mathbf{B}_{1/2}}{2m}\right)^2}, \tag{2.2}$$

where $\mathbf{B}_{1/2} \equiv \mathbf{B}(\mathbf{x}_{1/2})$. The variable $\mathbf{x}_{1/2}$ can then be solved iteratively.

For large time steps ($\delta t > 1$) the above solution fails to accurately capture all particle drifts. This is caused by numerical time step errors which result in the gyro-radius ρ_0 becoming larger than the magnetic field scale length $\rho_0 \left|\nabla B/B_0\right|$. Currently another approach [38] is used where the equations of motion are modified as

$$\frac{\mathbf{u}_1 - \mathbf{u}_0}{\delta t} = \frac{q}{m}\left(\mathbf{E}(\mathbf{x}_{1/2}) + \frac{\mathbf{u}_1 + \mathbf{u}_0}{2} \times \mathbf{B}(\mathbf{x}_{1/2})\right) - \mu \nabla B_{1/2}$$
$$\frac{\mathbf{x}_1 - \mathbf{x}_0}{\delta t} = \frac{\mathbf{u}_1 + \mathbf{u}_0}{2},$$

where μ, the magnetic moment, is defined as

$$\mu \equiv \frac{\left[\mathbf{u}_{1\perp} - \mathbf{u}_{0\perp}\right]^2}{8B_{1/2}}$$

where the subscript $\perp$ indicates variables perpendicular to the magnetic field. One can show with a few algebraic manipulations that this alternative definition of the magnetic moment is equivalent to

$$\mu = \frac{\mathbf{u}_\perp \Omega^2 \delta t^2}{8B_{1/2}(1 + \Omega^2 \delta t^2/4)},$$

where Ω is the cyclotron frequency. This definition of μ becomes negligible for small time steps and equal to the actual magnetic moment for large time steps. This additional term explicitly adds contributions from the ∇B force for large time steps, thus capturing all drift motion. As μ is dependent on $\mathbf{u}_1$, the new equations of motion must be solved twice, once for μ then once for $\mathbf{u}_1$.

As it is sufficiently accurate and fast for the simulations, in this thesis the first method of integration is used with a small time step. However, in future simulations the second method could be used to increase the time steps, as well as the total integration time.

2.2 Lyapunov Exponents

In order to properly compute the collisionless conductivity tensor, the chaotic regions of the systems of interest must be defined in order to avoid contributions from non-chaotic regions to the conductivity. It is expected that regions close to the magnetic null are to be chaotic, while regions far away are to be non-chaotic. In these chaotic regions the adiabatic invariants are not conserved, thus resulting in very interesting particle trajectories.

One of the primary tools for examining chaotic properties of systems is by the use of Lyapunov exponents, which measure the rate of divergence in phase-space of two trajectories with an initial infinitesimal separation. The spectrum of Lyapunov exponents in an n-dimensional phase space can best be described using an n-sphere defined by n different points around a central initial condition $\mathbf{x}_0$ [39]. The vectors that span from the initial condition to the points on the n-sphere form perpendicular vectors in the tangent space of the system. As the central point moves along in phase-space, the n-sphere moves along with it, governed by a linearized set of differential equations for the system. As time progresses, the n-sphere evolves into an n-ellipsoid due

to the increasing separation from the trajectory derived from the initial point and the n-sphere trajectories derived from the vectors in tangent space. The ith one-dimensional Lyapunov exponent, λ_i, is then defined as the length of the principal axis of the resulting ellipsoid,

$$\lambda_i = \lim_{t\to\infty} \frac{1}{t} \ln \frac{|\Delta \mathbf{r}_i(t)|}{|\Delta \mathbf{r}_i(0)|} = \lim_{N\to\infty} \frac{1}{N\tau} \sum_{m=0}^{m=N-1} \ln \frac{|\Delta \mathbf{r}_i((m+1)\tau)|}{|\Delta \mathbf{r}_i(m\tau)|},$$

where $\Delta \mathbf{r}_i(t)$ is the length of the ith vector in tangent space (or the ith principal axis of the n-ellipsoid) at time t, N is the number of simulation steps, τ is the time step, and, by convention,

$$\lambda_i \geq \lambda_{i+1}.$$

An n-dimensional phase space will have a maximum of n distinct one-dimensional Lyapunov exponents, though some may be repeated. In conservative Hamiltonian systems, if λ_i is a Lyapunov exponent, then $-\lambda_i$ is also a Lyapunov exponent, with the sum of all Lyapunov exponents summing to zero. The systems that are studied here have a five-dimensional phase space of three coordinate dimensions and two velocity ($v_\perp$ and $v_\parallel$) dimensions. As this system is Hamiltonian, there will be three distinct Lyapunov exponents with $\lambda_3 = 0$. A system is considered chaotic if $\lambda_1 > 0$, where λ_1 is denoted as the maximal Lyapunov exponent.

The jth-dimensional Lyapunov exponent can also be defined using the volume growth rate of the j-parallelotope formed the by the j first principal axises of the n-ellipsoid, which become a combination of j one-dimensional Lyapunov exponents. This is described formally as [40]

$$\lambda(e^j, \mathbf{x}) = \lim_{t\to\infty} \frac{1}{t} \ln \frac{||\Delta \mathbf{r}_1(t) \wedge \Delta \mathbf{r}_2(t) \wedge \cdots \wedge \Delta \mathbf{r}_j(t)||}{||\Delta \mathbf{r}_1(0) \wedge \Delta \mathbf{r}_2(0) \wedge \cdots \wedge \Delta \mathbf{r}_j(0)||},$$

where $\lambda(e^j, \mathbf{x})$ is the jth-dimensional Lyapunov exponent of some jth-dimensional subspace e^j in the tangent space of point $\mathbf{x}$ and $\wedge$ denotes the

exterior product. The norm of the exterior product can alternatively be represented by the Gram determinant [41],

$$||\Delta\mathbf{r}_1(t) \wedge \Delta\mathbf{r}_2(t) \wedge \cdots \wedge \Delta\mathbf{r}_j(t)||^2 = \\ - \begin{vmatrix} \langle \Delta\mathbf{r}_1(t), \Delta\mathbf{r}_1(t) \rangle & \langle \Delta\mathbf{r}_1(t), \Delta\mathbf{r}_2(t) \rangle & \dots & \langle \Delta\mathbf{r}_1(t), \Delta\mathbf{r}_j(t) \rangle \\ \langle \Delta\mathbf{r}_2(t), \Delta\mathbf{r}_1(t) \rangle & \langle \Delta\mathbf{r}_2(t), \Delta\mathbf{r}_2(t) \rangle & \dots & \langle \Delta\mathbf{r}_2(t), \Delta\mathbf{r}_j(t) \rangle \\ \vdots & \vdots & \ddots & \vdots \\ \langle \Delta\mathbf{r}_j(t), \Delta\mathbf{r}_1(t) \rangle & \langle \Delta\mathbf{r}_j(t), \Delta\mathbf{r}_2(t) \rangle & \dots & \langle \Delta\mathbf{r}_j(t), \Delta\mathbf{r}_j(t) \rangle \end{vmatrix},$$

where $\langle \ , \ \rangle$ denotes the interior product. The jth-dimensional Lyapunov exponent can take one of ${}_nC_j$ values, but in practice, as the principal axises are ordered by length, the jth-dimensional Lyapunov exponent is a sum of the first j one-dimensional Lyapunov exponents.

A method for computing the Lyapunov exponents from a system of differential equations was developed simultaneously by Benettin *et al.*[42, 43], and Shimada *et al.*[40]. Special numerical considerations must be taken into account when computing the Lyapunov spectrum. As the principal axises of the n-ellipsoid diverge exponentially for chaotic systems, long simulations run the risk of overflow problems. Also, for long simulations, the principal axes of the n-ellipsoid tend to fall along the direction of most rapid growth associated with the maximal Lyapunov exponent. Because of a lack of precision, this leads to the calculation of only the maximal Lyapunov exponent. These two problems can be easily circumvented using the Gram-Schmidt reorthonomalization (GSR) procedure, which creates the following ortronormal basis vectors in tangent space:

$$\begin{aligned} \Delta\mathbf{r}'_1 &= \frac{\Delta\mathbf{r}_1}{|\Delta\mathbf{r}_1|} \\ \Delta\mathbf{r}'_2 &= \frac{\Delta\mathbf{r}_2 - (\Delta\mathbf{r}_2 \cdot \Delta\mathbf{r}'_1)\Delta\mathbf{r}'_1}{|\Delta\mathbf{r}_2 - (\Delta\mathbf{r}_2 \cdot \Delta\mathbf{r}'_1)\Delta\mathbf{r}'_1|} \\ &\vdots \\ \Delta\mathbf{r}'_n &= \frac{\Delta\mathbf{r}_n - (\Delta\mathbf{r}_n \cdot \Delta\mathbf{r}'_{n-1})\Delta\mathbf{r}'_{n-1} - \cdots - (\Delta\mathbf{r}_n \cdot \Delta\mathbf{r}'_1)\Delta\mathbf{r}'_1}{|\Delta\mathbf{r}_n - (\Delta\mathbf{r}_n \cdot \Delta\mathbf{r}'_{n-1})\Delta\mathbf{r}'_{n-1} - \cdots - (\Delta\mathbf{r}_n \cdot \Delta\mathbf{r}'_1)\Delta\mathbf{r}'_1|}. \end{aligned}$$

This ensures that the vectors remain a certain size to avoid overflow errors, as well as preventing them to fall upon the same direction by keeping them perpendicular. This procedure should be applied frequently enough to ensure no numerical errors occur, but as it's computationally inexpensive, in practice it is applied after every time step.

As the direction of $\Delta\mathbf{r}'_1$ is never altered, it is free to seek out the direction of fastest growth. This vector is associated with the maximal Lyapunov exponent. As the direction of $\Delta\mathbf{r}'_2$ is always perpendicular to $\Delta\mathbf{r}'_1$ it is not free to seek out the direction of fastest growth. It is also not able to seek out the second most rapidly growing direction, as by applying the procedure at different frequencies different $\Delta\mathbf{r}'_2$'s will scan directions that are not in general parallel. However, the growth rate of the area of the parallelogram formed by $\Delta\mathbf{r}'_1$ and $\Delta\mathbf{r}'_2$ will be equivalent to the growth rate of the area formed by $\Delta\mathbf{r}_1$ and $\Delta\mathbf{r}_2$, corresponding to the 2nd-dimensional Lyapunov exponent. This can be seen by using a property of the exterior product [40], which can be written as

$$\Delta\mathbf{r}_1(t) \wedge \Delta\mathbf{r}_2(t) \wedge \cdots \wedge \Delta\mathbf{r}_j(t) = \bigwedge_j \Delta\mathbf{r}_j.$$

If U is the transformation that advances a particle's phase-space coordinates by one timestep and the sets $\{\Delta r_j\}$, $\{\Delta r'_j\}$ span the same subspace, then

$$\frac{\| \bigwedge_j U\Delta\mathbf{r}_j\|}{\| \bigwedge_j \Delta\mathbf{r}_j\|} = \frac{\| \bigwedge_j U\Delta\mathbf{r}'_j\|}{\| \bigwedge_j \Delta\mathbf{r}'_j\|}.$$

From this the n one-dimensional Lyapunov exponents can be calculated directly.

The equations of motion for the n-sphere are linearized by adding additional difference terms to Eqn.2.1, giving

$$\frac{d}{dt}\left(\mathbf{u} + \Delta\mathbf{u}\right) = \frac{q}{m}\left[\mathbf{E}(\mathbf{x} + \Delta\mathbf{x}) + (\mathbf{u} + \Delta\mathbf{u}) \times \mathbf{B}\left(\mathbf{x} + \Delta\mathbf{x}\right)\right].$$

As $\mathbf{E}$ and $\mathbf{B}$ are both linear in $\mathbf{x}$, they can be separated, giving

$$\frac{d\mathbf{u}}{dt} + \frac{d\Delta\mathbf{u}}{dt} = \frac{q}{m}\Big(\mathbf{E}(\mathbf{x}) + \mathbf{E}(\Delta\mathbf{x}) + \mathbf{u}\times\mathbf{B}(\mathbf{x}) \\ +\Delta\mathbf{u}\times\mathbf{B}(\mathbf{x}) + \mathbf{u}\times\mathbf{B}(\Delta\mathbf{x}) + \Delta\mathbf{u}\times\mathbf{B}(\Delta\mathbf{x})\Big).$$

Second order terms can be eliminated as well as the zeroth-order equation that has already been solved, giving

$$\frac{d\Delta\mathbf{u}}{dt} = \frac{q}{m}\left[\mathbf{E}(\Delta\mathbf{x}) + \Delta\mathbf{u}\times\mathbf{B}(\mathbf{x}) + \mathbf{u}\times\mathbf{B}(\Delta\mathbf{x})\right],$$

which are the final linearized equations of motion. The variables $\mathbf{x}$ and $\mathbf{u}$ are taken from the computation of the main particle trajectory. To determine the chaos region, we first define a time-dependent formulation of the maximal Lyapunov exponent:

$$\lambda_1(N) = \sum_{m=0}^{m=N-1} \ln\frac{|\Delta\mathbf{r}_1((m+1)\tau)|}{|\Delta\mathbf{r}_1(m\tau)|},$$

where τ is the time-step and N is the Nth-step of the simulation. The chaos region is defined as the region on the particle trajectory where

$$\frac{d}{dt}\lambda_1(N) \approx 1.$$

In practice, 100 particles are used in simulations lasting 100,000 timesteps to determine the chaos region.

2.3 Evaluation of Conductance

2.3.1 Kubo Conductivity

The Kubo Conductivty is derived by applying the fluctation-dissipation theorem to currents in eletromagnetic-fields. The fluctuation-dissipation theorem states that the linear response to dissapative processes in non-equilibrium systems can be predicted by the fluctuation properties when the same system is in equilibrium, providing the magnitude of the perturbation to the distribution

function is small. In this section the fluctuation-dissipation will be derived quantum-mechanically following Kubo's derivation in [23, 24], after which the classical equations can be obtained by taking the limit $\hbar \to 0$.

Consider an isolated system with a Hamiltonian $\mathscr{H}$ and density matrix ρ which satisfies $[\mathscr{H}, \rho] = 0$, where the brackets indicate the commutator. Let $\rho'(t)$ be the density of the perturbed system with an additional Hamiltonial term $\mathscr{H}' = -AF(t)$. Here, $F(t)$ is the perturbing force and A represents the dynamical quantity conjugate to that force. The perturbed system obeys the equation

$$\frac{d}{dt}\rho'(t) = \frac{1}{i\hbar}\left[\mathscr{H} + \mathscr{H}'(t), \rho'(t)\right] \tag{2.3}$$

with initial condition

$$\rho'(-\infty) = \rho.$$

If the perturbation is small and applied adiabatically at $t = -\infty$, $p'(t)$ can be expanded as

$$\rho'(t) = \rho + \Delta\rho(t). \tag{2.4}$$

which, after dropping second order terms, gives

$$i\hbar\frac{\partial \Delta\rho}{\partial t} = [\mathscr{H}, \Delta\rho] - F(t)[A, \rho]. \tag{2.5}$$

By multiplying both sides by an integrating factor on the left and its complex conjugate on the right, the solution is found to be

$$\Delta\rho(t) = -\frac{1}{i\hbar}\int_{-\infty}^{t} \exp(-i(t-t')\mathscr{H}/\hbar)[A, \rho]\exp(i(t-t')\mathscr{H}/\hbar)F(t')dt'. \tag{2.6}$$

Suppose the response of the perturbation to the system is observed through the change $\Delta B(t)$ of a physical quantity $B(q, p)$, where q and p are the canonical coordinates and momenta, respectively. The expectation value of $\Delta B(t)$ would

then be given as

$$\Delta B(t) = \mathrm{Tr}\Delta\rho(t)B(q,p) \tag{2.7}$$

$$= -\frac{1}{i\hbar}\mathrm{Tr}\int_{-\infty}^{t}\exp(-i(t-t')\mathscr{H}/\hbar)[A,\rho]\exp(i(t-t')\mathscr{H}/\hbar)BF(t')dt'. \tag{2.8}$$

where Tr signifies the trace operation in quantum mechanics, which reduces to a phase-space integration in classical mechanics. If we use the Heisenberg representation of B, that is, transforming $B(p,q) \rightarrow B(t)$ where $B(t)$ satisfies the equation

$$\dot{B}(t) = \frac{1}{i\hbar}[B(t),\mathscr{H}], B(0) = B,$$

then Eqn. 2.8 simplifies to

$$\Delta B(t) = -\frac{1}{i\hbar}\mathrm{Tr}\int_{-\infty}^{t}[A,\rho]B(t-t')F(t')dt'. \tag{2.9}$$

We define the linear response function $\phi_{BA}(t)$ as

$$\phi_{BA}(t) = -\frac{1}{i\hbar}\mathrm{Tr}[A,\rho]B(t), \tag{2.10}$$

which reduces in the classical limit to

$$\phi_{BA}(t) = -\int d\Gamma(A,f)B(t). \tag{2.11}$$

Here, f is the classical distribution function, the integral is over phase-space and the parentheses represent the Poisson bracket,

$$(A,B) = \sum\left(\frac{\partial A}{\partial q}\frac{\partial B}{\partial p} - \frac{\partial A}{\partial p}\frac{\partial B}{\partial q}\right). \tag{2.12}$$

The response function can be used to simplify 2.9 even further to

$$\Delta B(t) = \int_{-\infty}^{t}\phi_{BA}(t-t')F(t')dt'. \tag{2.13}$$

Equation 2.13 can be further simplified if we consider the identity

$$\begin{aligned}[A,\exp(-\beta\mathscr{H})] &= \exp(-\beta\mathscr{H})\int_0^\beta \exp(\lambda\mathscr{H})[\mathscr{H},A]\exp(-\lambda\mathscr{H})d\lambda \\ &= \frac{\hbar}{i}\exp(-\beta\mathscr{H})\int_0^\beta \exp(\lambda\mathscr{H})\dot{A}\exp(-\lambda\mathscr{H})d\lambda \\ &= \frac{\hbar}{i}\exp(-\beta\mathscr{H})\int_0^\beta \dot{A}(-i\hbar\lambda)d\lambda\end{aligned} \tag{2.14}$$

where $\beta = 1/k_{\mathrm{B}}T$, k_{B} is the Boltzmann constant and T is the temperature of the system. The Heisenberg representation has been used in the above derivation. Eqn. 2.14 is equivalent to

$$[\rho, A] = i\hbar \int_0^\beta \rho \dot{A}(-i\hbar\lambda) d\lambda.$$

From here the response function becomes

$$\phi_{BA}(t) = \frac{1}{i\hbar}\mathrm{Tr}[\rho, A]B(t) \tag{2.15}$$

$$= \int_0^\beta \mathrm{Tr}\rho\dot{A}(-i\hbar\lambda)B(t)d\lambda \tag{2.16}$$

$$= -\int_0^\beta \mathrm{Tr}\rho A(-i\hbar\lambda)\dot{B}(t)d\lambda \tag{2.17}$$

where the cyclic property of the trace has been used. For shorthand, we use

$$\mathrm{Tr}\rho(\dot{A}(-i\hbar\lambda), B(t)) = \left\langle (\dot{A}(-i\hbar\lambda), B(t)) \right\rangle.$$

In classical mechanics, the angular brackets signify an ensemble average. The force is assumed to be periodic,

$$F(t) = \Re F_0 e^{i\omega t}$$

then we can define the complex admittance $\chi_{BA}(\omega)$ as the Fourier transform of the response function. This approximation is valid for travelling waves with long wavelengths $k \ll \omega$. The response $\Delta B(t)$ of $F(t)$ can now be expressed as

$$\Delta B(t) = \Re \chi_{BA}(\omega) K_0 e^{i\omega t} \tag{2.18}$$

with

$$\chi_{BA}(\omega) = \int_0^\infty e^{-i\omega t}\phi_{BA}(t)dt \tag{2.19}$$

$$= \int_0^\infty e^{-i\omega t} \int_0^\beta \left\langle (\dot{A}(-i\hbar\lambda), B(t)) \right\rangle d\lambda dt \tag{2.20}$$

where $\beta = (k_{\mathrm{B}}T)^{-1}$Eqn.2.20 is known as the fluctuation-dissipation theorem. In the classical limit, we have

$$\chi_{BA}(\omega) = \beta \int_0^\infty e^{-i\omega t} \left\langle \dot{A}(0), B(t) \right\rangle dt. \tag{2.21}$$

If the system is ergodic, the angular brackets become the correlation of quantities A and B. To arrive at the Kubo conductivity, we consider a perturbing electric field $\mathbf{E}(t)$ with the additional Hamiltonian term

$$\mathscr{H}'(t) = -\sum_i e_i \mathbf{r}_i \cdot \mathbf{E}(t) \tag{2.22}$$

where e_i and r_i are the charge and the position vector of the ith particle, respectively. The linear response function of the current in the μ-direction when an electric field is applied in the ν-direction is

$$\phi_{BA}(t) = \left\langle e_i \frac{d}{dt} r_\nu \Big|_0 , J_\mu(t) \right\rangle \tag{2.23}$$

$$= \langle J_\nu(0), J_\mu(t) \rangle \tag{2.24}$$

where

$$J_\mu = \sum e_i \dot{x}_{i\mu}.$$

This results in the conductivity

$$\sigma_{\mu\nu}(\omega) = \chi_{J_\mu J_\nu}(\omega) = \beta \int_0^\infty e^{-i\omega t} \langle J_\nu(0), J_\mu(t) \rangle . \tag{2.25}$$

Eqn. 2.25 is known as the Kubo conductivity, which is an exact expression for the electrical conductivity tensor $\sigma_{\mu\nu}(\omega)$.

The correlation in Eqn. 2.25 is defined as

$$\langle J_\nu(0), J_\mu(t) \rangle = \frac{1}{N} \sum_{i=1}^{N} \frac{1}{T} \int_0^{T-\tau} q_i^2 u_\nu(t) u_\mu(t+\tau) d\tau. \tag{2.26}$$

A useful theorem to note here is the cross-correlation theorem,

$$\int_{-\infty}^{\infty} \bar{A}(t) B(t+\tau) d\tau = \frac{1}{2\pi} \int_{-\infty}^{\infty} \bar{A}(\omega) B(\omega) e^{-i\omega t} d\omega \tag{2.27}$$

which states that the correlation of variables A and B is simply the inverse fourier transform of the power spectrum between variables A and B, where the overbar signifies the complex conjugate. When $A = B$, this theorem reduces to the Wiener-Khinchin theorem. From this the Kubo conductivity is simply proportional to the power spectrum of velocity v_μ and v_ν. A corollary of this is that when the Kubo conductivity is integrated over all frequencies,

$$\int_0^\infty d\omega \mathrm{Re}\,\sigma(\omega) = \frac{nq^2}{m}\frac{\pi}{2}, \tag{2.28}$$

which can be seen by taking the inverse fourier transform of the power spectrum with $t = 0$.

2.3.2 Mean Drift method

The mean-drift method used to compute the DC-conductivty by Numata *et al.*[2] is based on a dissipative approach. The dissipative equation used to fit the average **z** velocity is

$$\hat{\rho}\frac{d\hat{\bar{v}}}{d\hat{t}} = m_\mathrm{A}\hat{e}_z - \hat{\nu}_\mathrm{eff}\hat{\bar{v}}$$

where $\hat{\bar{v}}$ is the normalized average velocity in the **z** direction, $\hat{\rho}$ is an effective mass normalized by the ion mass, and $\hat{\nu}_\mathrm{eff}$ is an effective collision frequency normalized by ω_c which is to be determined. Here, $\hat{\rho} = 1$. The solution to this equation is

$$\hat{\bar{v}} = \frac{m_\mathrm{A}\hat{e}_z}{\hat{\nu}_\mathrm{eff}}\left[1 - \exp\left(-\frac{\hat{\nu}_\mathrm{eff}}{\rho}\hat{t}\right)\right]. \tag{2.29}$$

Using Ohm's law, we define an effective resistivity η_eff

$$E_z = \eta_\mathrm{eff} j_z = \eta_\mathrm{eff} nq\hat{v}_\mathrm{sat}, \tag{2.30}$$

where n is the density and $\hat{v}_\mathrm{sat}$ is the defined as the asymptotic limit of the average z velocity for large times, i.e. from Eqn.(2.29)

$$\hat{v}_\mathrm{sat} = \frac{m_\mathrm{A}\hat{e}_z}{\hat{\nu}_\mathrm{eff}}.$$

From this, one can show that the resistivity is

$$\frac{\eta_{\text{eff}}}{\mu_0} = \lambda_i^2 \omega_c \hat{\nu}_{\text{eff}}. \tag{2.31}$$

where $\lambda_i = c/\omega_p$ is the ion skin depth and ω_p is the ion plasma frequency. The conductance is simply the reciprocal of the resistivity. This effective collisional resistivity can be related to the Kubo DC-conductivity through

$$\hat{\nu}_{\text{eff}}^{-1} = \sigma_{zz}(0)\mu_0\lambda_i^2\omega_{ci} = N^{-1}\beta \sum_{i=1}^{N} \int_0^\infty d\tau \overline{u_z(t)u_z(t-\tau)}. \tag{2.32}$$

It is important to note that while the mean-drift method gives a local conductivity near the region of chaos, the Kubo conductivity effectively gives a global conductivity for the whole system, as it is averaged over all space.

In order to compare Eqn. 2.31 to the conductivty by Speiser in [22], it is important to note that Numata *et al.* find that their resistivity is inversely proportional to the applied electric field. However, Numata et al. state that the particle staying time $\hat{\tau}_1$ is equal to the reciprocal of the Alfvén Mach number m_{A}. From this it can be shown that Eqn. 2.31 is equivalent to

$$\begin{aligned} \sigma_{\text{eff}} &= \frac{\tau_1}{\mu_0 \lambda_i^2} \\ &= \frac{\tau_1 \omega_p^2}{\mu_0 c^2} \\ &= \frac{n e^2 \tau_1}{m}, \end{aligned} \tag{2.33}$$

where τ_1 is the unnormalized particle staying time. Eqn. 2.33 is consistent with Speiser's formulation of the conductivity.

Chapter 3

Two-dimensional null results

In order to properly understand the results of the Kubo conductivity, both the regular and chaotic equilibrium dynamics of the two-dimensional null must be characterized. Speiser [22] considers three cases: regular (periodic) orbits in which the adiabatic invariant μ is conserved, chaotic orbits in which μ is not conserved, and orbits which observe fluctuating periodic motion in which μ is not always conserved. The third case can be considered as a combination of the first two cases and will not be considered independently.

The two-dimensional null model we consider here is one proposed by Numata et al.[2]:

$$\mathbf{B} = \begin{cases} [B_0 (y \mp l_y), B_0 x/l_x, 0] & (\pm y > l_y), \\ (0, B_0 x/l_x, 0) & (|y| \leq l_y), \end{cases} \tag{3.1}$$

where $L_x = L_y = 1$. For simplicity, the magnetic field is normalized to B_0.

3.1 Regular dynamics

Regular orbits of the two-dimensional null are those that the adiabatic invariant μ is conserved, which are typically orbits far away from the magnetic null. Two motions characterize these orbits, the first being the bounce motion around the hyperbolic field lines of $\mathbf{B}$[34], which are given by solving the differential equations

$$\frac{dx}{B_x} = \frac{dy}{B_y},$$

which give the field line

$$x = \sqrt{y^2 + C^2}$$

outside the L_y region, where C is a constant and $L_y = 0$. Field lines in the region $|y| < L_y$ are simply straight lines that travel from $-L_y$ to L_y with constant x. As a particle travels along a field line, it experiences the mirror force

$$\mathbf{F} = -\mu \nabla B = -\frac{\mu b_0}{L_x} \frac{x\hat{x} + y\hat{y}}{\sqrt{x^2 + y^2}} \tag{3.2}$$

where $B = |\mathbf{B}|$ is the magnitude of the magnetic field. Here, $L_y = 0$ for simplicity. Far along the field lines, the mirror force becomes a constant acceleration which brings particles back towards the null in parabolic orbits. As shall be seen, this is a feature for all linear magnetic nulls. Particles in the region $|y| < L_y$ travel at constant velocities along field lines.

The bounce frequency f_{B} along the field lines can be calculated directly. For $L_y = 0$, the element of arc length along the field line is

$$ds^2 = dx^2 + dy^2 = dx^2 + \frac{x^2}{x^2 + C^2} dx^2 = \frac{2y^2 + C^2}{y^2 + C^2} dx^2. \tag{3.3}$$

By using conservation of μ, the parallel velocity to the magnetic field is

$$v_{\parallel}^2 = v^2 - v_{\perp}^2 = v^2 \left[1 - \frac{B}{B_0} \sin^2(\theta_0) \right] \tag{3.4}$$

where $\sin^2(\theta_0) = v_{\perp 0}^2 / v_0^2$ and $B_0, v_0, v_{\perp 0}$ are the initial magnetic field, total and perpendicular velocities, respectively. The bounce frequency f_{B} can now be calculated as

$$f_{\mathrm{B}} = \frac{4}{v} \int_0^{y_{\mathrm{m}}} \frac{\sqrt{2y^2 + C^2}}{\sqrt{y^2 + C^2} \sqrt{1 - \sin^2 \theta_0 \frac{\sqrt{2y^2 + C^2}}{\sqrt{y_0^2 + C^2}}}} dx \tag{3.5}$$

where y_m is the mirroring point where $v_{\parallel} = 0$. For orbits that pass through the region $|y| < L_y$, an extra term $4L_y / v_{\parallel 0}$ is added, where $v_{\parallel 0}$ is the parallel velocity within the region proper. The above equation applies to the region

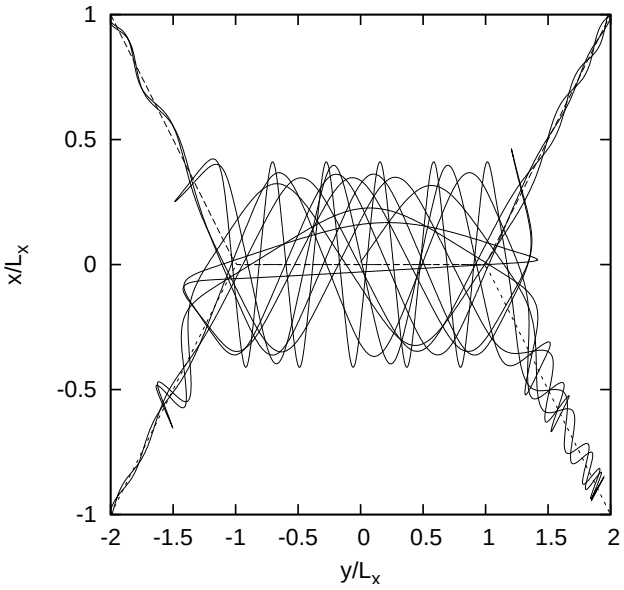

Figure 3.1: Typical particle orbit (solid line) in the Y-shaped magnetic field (dotted line) with $L_x = L_y$ and $v_s = 0.05 v_{\rm A}$

above and below the null line, while the region beside the null line is simply the above with all y variables interchanged with x variables. To test Eq. 3.5, we use a particle with initial conditions $L_y = 1$, $C = 10$, $\sin\theta_0 = 0.581$, and $y_0 = 0$. This gives $y_m \approx 19.7$ and $f_{\rm B} = 3.94 \times 10^{-4}$, which should lead to a delta-function peak at $\omega_{\rm B} = 2\pi f_{\rm B} = 2.47 \times 10^{-3}$ in the $\sigma_{yy}(\omega)$ conductivity and a delta function peak at $\omega = 2\omega_{\rm B}$ in the $\sigma_{xx}(\omega)$ conductivity. This agrees with simulation results.

The second motion that characterizes regular orbits is the ∇B-drift,

$$\mathbf{u}_{\nabla B} = \frac{\mu}{q}\frac{\mathbf{B}\times\nabla B}{B^2} = \begin{cases} \mu q^{-1} x^{-1}\hat{z} & (\pm y > l_y), \\ \mu q^{-1} B^{-3}\left[(y \mp L_y)^2 - x^2\right]\hat{z} & (|y| \le l_y), \end{cases} \tag{3.6}$$

This results in a delta-function peak at the DC ($\omega = 0$) component in the σ_{zz} conductivity. As $\mathbf{u}_{\nabla B}$ is inversely proportional to the xy-coordinates at large distances away from the magnetic neutral point, the z-drift velocity is negligible for regular orbits. Apart from the two motions mentioned about, peaks are also expected around the cyclotron frequency $\omega = qB/m$ for all diagonal components of the conductivity tensor.

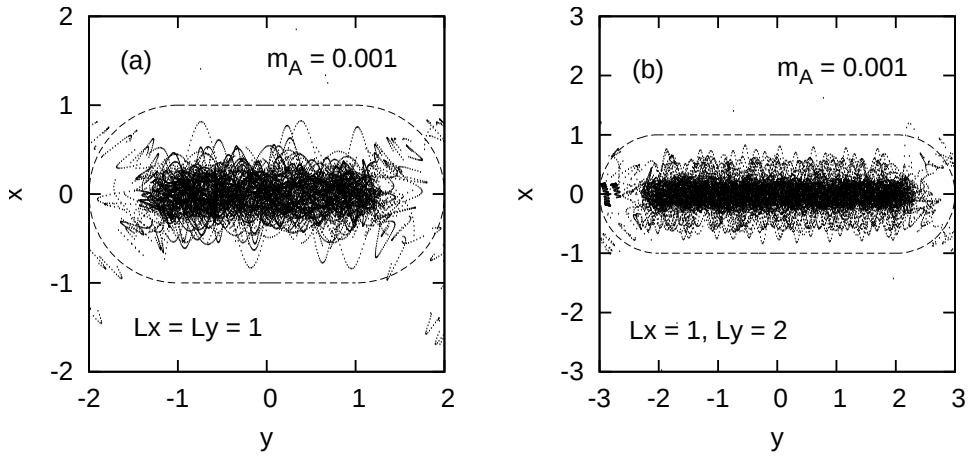

Figure 3.2: Chaotic particle trajectories which define the chaos region for the two-dimensional null with $m_{\rm A} = 0.001$, $L_x = 1$, $L_y = 2$ (a) and $L_y = 1$ (b). Dashed lines indicate the zone of chaos defined in [2].

3.2 Chaotic dynamics

Fig. 3.1 shows a typical orbit of a particle near the chaos region, defined by [2]. Particles that leave the chaos region eventually return due to the mirror force along the field lines. As the mirror force on the particle is directly proportional to the magnetic moment μ, the trip times may vary considerably as the value of μ will not be conserved once the particle re-enters the chaos region. The conductivity tensor components for these trajectories contain a spectrum of frequencies which vary considerably depending on the initial conditions, which reflects the sensitivity of chaotic motion.

Fig. 3.2 show the results for determining the chaos region using the maximal Lyapunov exponent for the $L_x = L_y = 1$ null system (a) and the $L_x = 1, L_y = 2$ null system (b), computed by tracking the trajectories of 50 particles over 50000 time steps. These results agree with the chaos region defined in Numata and Yoshida [2]. The chaos region is best described as a stadium-shaped region with a rectangle centered around the origin with major length $2L_y$ on the y-axis and minor length $2L_x$ on the x-axis with two half-circles of radius L_x on either side.

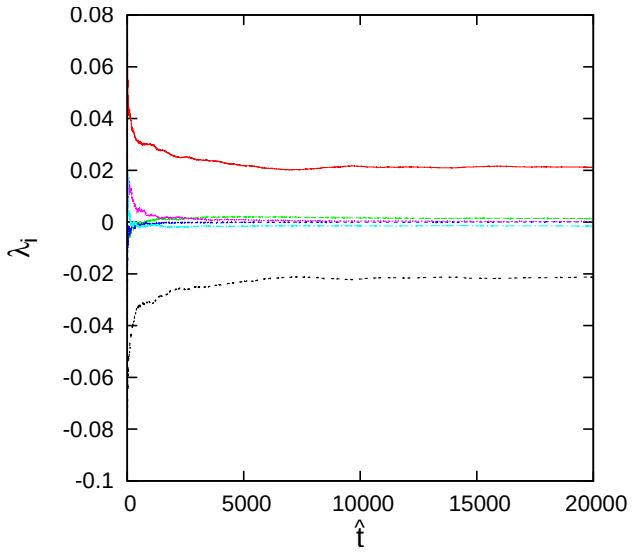

Figure 3.3: Typical evolution of the Lyapunov spectrum cotaining six exponents for an average of ten particles.

Fig. 3.3 show the typical evolution of the Lyapunov spectrum for an average of 10 particles over two million timesteps. All six exponents converge to a definite value for large t, with $\lambda_i = -\lambda_{6-i}$, $i = 1, 2, 3$. Computation of the Lyapunov spectrum averaged over 100 particles show that the three positive Lyapunov exponents are $\lambda_1 \approx 0.02$, $\lambda_2 \approx 0.001$, and $\lambda_3 = 0$, which indicate chaotic motion.

3.3 Conductivity results

Conductivity computations were carried out over 2^{21} time steps using 30000 particles with velocities drawn from a Maxwellian distribution with $v_{\mathrm{T}} = 0.05 v_{\mathrm{A}}$. Four cases of initial positions were used, with three cases on specific points in the chaos region whereas the fourth case involved particles uniformly distributed over the whole region. The positions are tabulated in Table 3.1. Each case was run five times with a different random seed to provide statistics for error analysis. Care must be taken to determine which points in the frequency range represent sufficiently sampled frequencies. A range of frequen-

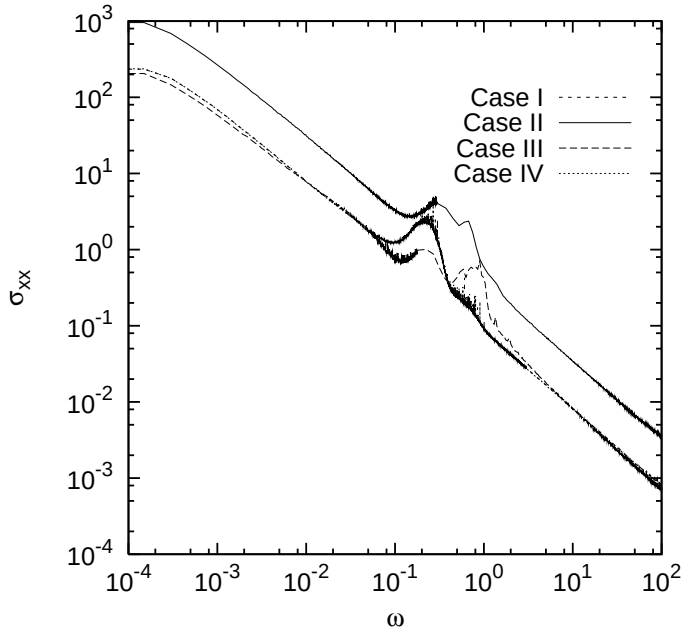

Figure 3.4: The conductivity tensor component $\sigma_{xx}(\omega)$ in a log-log scale. ω and σ_{xx} are in reduced units. Case IV follows the curve of Case I.

cies, defined by a minimum and a maximum frequency, can be determined by both the timestep and the maximum integration time. The maximum frequency is given by the Nyquist frequency

$$\omega_{\max} = \frac{\pi}{\Delta t} \approx 300,$$

while the minimum frequency is given by the Nyquist rate

$$\omega_{\min} \approx \frac{\pi}{N\Delta t} = 2 \times 10^{-4}.$$

In practice, frequencies that fall within a factor of 4 of these cut-offs are also considered undersampled. In all simulations, $L_x = L_y = 1$.

	$\hat{\mathbf{x}}_0$
Case I	$(0, 0, 0)$
Case II	$(0, 0.5, 0)$
Case III	$(0.5, 0, 5, 0)$

Table 3.1: Initial positions in reduced units for the first three cases.

Fig. 3.4 shows the conductivity tensor component $\sigma_{xx}(\omega)$ on a log-log scale in reduced units using one run for each case. Simulations of varying time steps

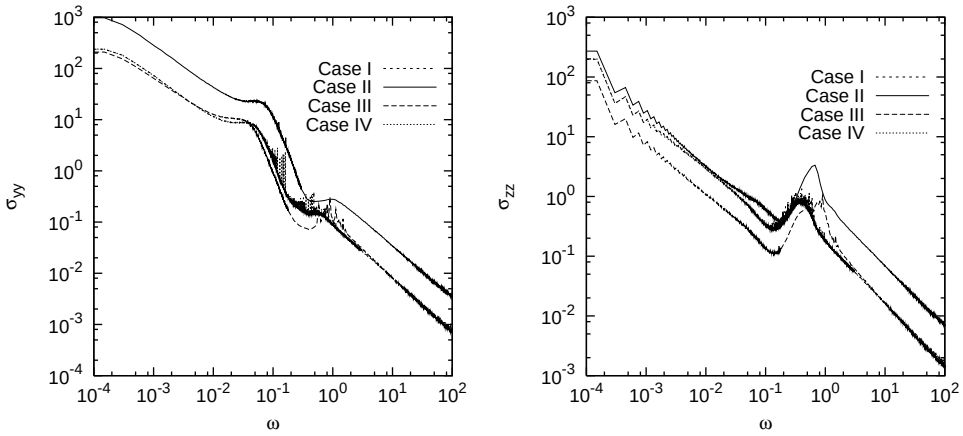

Figure 3.5: The conductivity tensor components $\sigma_{yy}(\omega)$ (a) and $\sigma_{zz}(\omega)$ (b) in a log-log scale. ω and σ_{xx} are in reduced units. Case IV follows the curve of Case I.

show the curve for frequencies below the cyclotron frequency $\omega_c \approx 1$ converge to a power law with a unique exponent for all cases. Case II exhibits a different pre-factor than the other cases. Frequencies around the cyclotron frequency $0.1 < \omega_c < 5$ show a series of definite peaks above the power law line, though the locations of these peaks change depending on the initial position of the particles.

	Case I	Case II
a_{xx}	$(1.126 \pm 0.005) \times 10^{-1}$	$(1.143 \pm 0.08) \times 10^{-1}$
b_{xx}	$(-9.233 \pm 0.004) \times 10^{-1}$	$(-9.208 \pm 0.0013) \times 10^{-1}$
a_{yy}	$(3.16 \pm 0.03) \times 10^{-1}$	$(3.22 \pm 0.05) \times 10^{-1}$
b_{yy}	$(-7.794 \pm 0.014) \times 10^{-1}$	$(-7.77 \pm 0.02) \times 10^{-1}$
a_{zz}	$(1.000 \pm 0.008) \times 10^{-1}$	$(1.013 \pm 0.010) \times 10^{-1}$
b_{zz}	$(-7.370 \pm 0.013) \times 10^{-1}$	$(-7.357 \pm 0.0012) \times 10^{-1}$
	Case III	Case IV
a_{xx}	$(4.23 \pm 0.08) \times 10^{-1}$	$(1.56 \pm 0.03) \times 10^{-1}$
b_{xx}	$(-9.293 \pm 0.004) \times 10^{-1}$	$(-8.51 \pm 0.03) \times 10^{-1}$
a_{yy}	$(1.060 \pm 0.015) \times 10^{-1}$	$(4.7 \pm 0.2) \times 10^{-1}$
b_{yy}	$(-8.02 \pm 0.02) \times 10^{-1}$	$(-7.07 \pm 0.06) \times 10^{-1}$
a_{zz}	$(5.91 \pm 0.09) \times 10^{-2}$	$(2.58 \pm 0.03) \times 10^{-2}$
b_{zz}	$(-8.63 \pm 0.03) \times 10^{-1}$	$(-8.051 \pm 0.0008) \times 10^{-1}$

Table 3.2: Parameters for the diagonal component power laws of the conductivity tensor in reduced units.

Fig. 3.5 shows the conductivity tensor components $\sigma_{yy}(\omega)$ (3.5(a))and $\sigma_{zz}(\omega)$(3.5(b)) on a log-log scale in reduced units using one run for each case. As with $\sigma_{xx}(\omega)$, simulations of varying time steps show the curve for frequencies below the cyclotron frequency converge to a power law, with additional peaks appearing in the cyclotron frequency range. In all cases, $\sigma_{zz}(\omega)$ displays a jaggedness for small frequencies $\omega \ll \omega_c$. This is characteristic of a numeric delta function $\hat{v}_z^2\delta(\omega)$, where $\hat{v}_z^2$ is the average squared velocity in the z direction. The jaggedness of this curve can be seen by taking the power spectrum of a constant

$$\begin{aligned}
|F(\omega)|^2 &= \frac{1}{T}\left|\int_0^T \hat{v}_z e^{i\omega t}dt\right|^2, \\
&= 2\hat{v}_z^2 T\frac{\left(e^{i\omega t}-1\right)\left(e^{-i\omega T}-1\right)}{\omega^2T^2}, \\
&= 2\hat{v}_z^2 T\frac{1-\cos(\omega T)}{\omega^2T^2}, \\
&= 2\hat{v}_z^2 T\ \frac{1-\cos(\pi n)}{(\pi n)^2}.
\end{aligned}$$

where

$$\lim_{\omega\to 0}|F(\omega)|^2 = \hat{v}_z^2 T.$$

Here, T is the integration time, n is the iteration step, and, as the integrated time interval is $2T$ to avoid wrap-around interference, $\omega = \pi/n\Delta\hat{t}$. The above equations enables the direct calculation of the average squared z-velocity from the conductivity without the need of integrating over the delta function. It is important to note that $\hat{v}_z^2$ is not a velocity associated with any particular current, as it is an average of squared velocities. In practice, the average z velocity is zero. The average squared z-velocity is tabulated in Tab. 3.3.

The parameters for all power laws $\sigma_{\mu\nu}(\omega) = a_{\mu\nu}\omega^{b_{\mu\nu}}$ are tabulated in Tab. 3.2. For Case IV, the Gaussian function $A_{\mu\nu}e^{-(\omega-\omega_{0\mu\nu})^2/\Delta\omega_{\mu\nu}}$ was used to fit peaks near the cyclotron frequency after the power laws were subtracted from the original conductivity curves. The $\sigma_{yy}(\omega)$ and $\sigma_{zz}(\omega)$ conductivity

curves were fitted using a single Gaussian function, while the $\sigma_{xx}(\omega)$ case was fitted with three Gaussian functions. The parameters for the Gaussian functions are tabulated in Tab. 3.4.

	$\overline{v_z^2}$
Case I	$(1.182 \pm 0.011) \times 10^{-4}$
Case II	$(1.127 \pm 0.017) \times 10^{-4}$
Case III	$(1.675 \pm 0.011) \times 10^{-4}$
Case IV	$(5.02 \pm 0.11) \times 10^{-5}$

Table 3.3: Average square-velocity in the zz direction for all cases.

Non-diagonal components of the conductivity tensor $\sigma_{\mu\nu}$ are characterized by a noise for small values of ω which eventually disappears for larger values of ω. As no consistent trend appears between any of the five test runs, the off-diagonal elements of the conductivity tensor $\sigma_{\mu\nu}$ are considered to be zero.

$\mu\nu$	$A_{\mu\nu}$	$\Delta\omega_{\mu\nu}$	$\omega_{0\mu\nu}$
xx_1	0.2250 ± 0.0014	$(9.0 \pm 0.6) \times 10^{-3}$	0.496 ± 1.6
xx_2	0.49 ± 0.03	$(6.2 \pm 0.3) \times 10^{-2}$	0.792 ± 0.003
xx_3	-0.463 ± 0.009	$(6.4 \pm 0.9) \times 10^{-3}$	$(9.28 \pm 0.13) \times 10^{-2}$
yy	4.46 ± 0.07	$(3.66 \pm 0.06) \times 10^{-6}$	$(3.262 \pm 0.007) \times 10^{-2}$
zz	0.92 ± 0.02	0.174 ± 0.003	0.732 ± 0.003

Table 3.4: Parameters for the Gaussian functions applied to the conductivity curves in Case IV.

3.4 Discussion

To better understand the results of the Kubo conductivity, it will be necessary to compare the above results with other conductivities, such as those derived from the mean-drift method, as well as those defined by Speiser [22]. A discrepancy between these conductivities can immediately be noticed from the fact that the Speiser conductivities as well as the mean-drift conductivity yield finite, non-zero DC values of the conductivity tensor, while the Kubo-method

diverges for $\omega = 0$, though this divergence in itself is not a problem, as an infinite conductivity simply implies no resistivity.

In order to explain these discrepancies, the theory behind the conductivities, as well as their physical meaning, must be compared. Speiser defines three conductivities in [22], all with the form

$$\sigma_s = \frac{ne^2}{m}\tau_s \tag{3.7}$$

where τ_s is an effective collision time of the system. One of the conductivities defined is a collisional conductivity, with the two others being non-collisional. The first non-collisional conductivity is based on the finite average lifetime of particles inside the current sheet layer, where particles typically diffuse. Here, the particles are freely accelerated by the applied electric field during their lifetimes. Once these particles leave the current sheet layer, they resume regular motion and the acceleration ceases. The total acceleration is simply the magnitude of the electric field multiplied by the average particle time life. The second conductivity defined by Speiser is related to the cyclotron motion which induces the familiar drift velocity

$$v_{\mathbf{E}} = \frac{\mathbf{E} \times \mathbf{B}}{B^2}, \tag{3.8}$$

which results in an effective collision time

$$\tau_g = \frac{m}{qB_\perp} = \frac{1}{\omega_c} \tag{3.9}$$

which is equal to the reciprocal of the cyclotron frequency. Here, $B_\perp$ is the magnitude of the magnetic field perpendicular to that of the electric field. To calculate the total conductivity of the system, Mathiessen's rule is used, i.e.

$$\sigma_{\text{total}} = \left(\sum_s \sigma_s^{-1} \right)^{-1}, \tag{3.10}$$

where σ_s is a conductivity of type s. Speiser states that, in practice, one can simply use the conductivity of smallest order, which reflects Eq. 3.10.

As mentioned in Sec. 2.3.2, the mean-drift method for computing the DC-conductivity follows the same form as Speiser's in Eq. 3.7, where the effective collision time is equivalent to the average staying time of the particle in the chaos region. Numata *et al.* state that this time, in reduced units, is equal to the reciprocal of the Alfvèn Mach number m_{A}, which gives the magnitude of the $\mathbf{E} \times \mathbf{B}$ drift velocity. This is derived from the reduced units $\mathbf{B} = b_0 \hat{\mathbf{b}}$ and $\mathbf{E} = v_{\mathrm{A}} m_{\mathrm{A}} b_0 \hat{\mathbf{e}}$, where hatted variables signify unitless quantities and v_{A} is the Alfvèn velocity. It is easy to see that, in reduced units,

$$\frac{v_{\mathbf{E}}}{v_{\mathrm{A}}} = \hat{v}_{\mathbf{E}} = \frac{\hat{e}}{\hat{b}} = m_{\mathrm{A}}. \tag{3.11}$$

If m_{A} is small, the $\mathbf{E} \times \mathbf{B}$ is also small. This allows the particles to stay in the zone of chaos for long periods of time. As m_{A} is increased, the drift velocity increases which results in more energetic particles leaving the zone of chaos sooner. Providing $l_y/l_x \lesssim 10$, the relation $\hat{\tau}_1 \approx m_{\mathrm{A}}^{-1}$ holds. Numata states that to ensure that chaotic processes play a significant role in the conductivity, $\hat{\tau}_1$ must be sufficiently large compared to the maximal Lyapunov exponent. This requires that $m_{\mathrm{A}} \lesssim 10^{-2}$.

The Kubo-conductivity is a formulation of the conductivity based on the time-averaged auto-correlation of component velocities over all lag times. As shown in Sec. 2.3.1 this is equivalent to the power spectrum of equilibrium component velocities. Unlike the conductivity used by Speiser and Numata, which is based on finite particle lifetimes, the Kubo conductivity must be integrated over all time. As noted in Holland and Chen [29], this leads to sensitivity of the the low-frequency ($\omega \gtrsim 0$) conductivity tensor to the total simulation time T. However, it was found that for increasing time-step the conductivity tensor for the two-dimensional linear null approached power laws for low frequency.

The two main contributions to the conductivity were from the cyclotron

frequency as well as the bounce frequency for trajectories to and from the null region, which reflects the fact that particles spend the majority of the simulation in non-chaotic adiabatic regions, as stated in [29]. The small amount of time spent in the chaos region, however, greatly affects the results of the conductivity tensors, as in this region the first adiabatic invariant μ is not-conserved, which results in a broad power spectrum. Conversely, regular particle orbits drawn from a Maxwellian result in a bounce frequency peak around some mean value. This bounce-frequency contribution to the conductivity is not captured in the Speiser formulation of the conductivity.

Simulations with constant $\mathbf{E}$ field were ran to make comparisons to the approach in Numata *et al.* [2]. It is important to note that neither initial velocities nor particle positions are stated for any of the simulations performed in that study. It is found that the saturation velocity $\hat{v}_z$ is strongly dependent on the initial temperature of the velocity distribution. For large time scales, particles escape in the positive y region of the x-point, where the $\mathbf{E} \times \mathbf{B}$ drift velocity drives the particle away from the magnetic null line.

It is important to compare the magnitude of the AC-conductivity to the DC conductivities mentioned above. For the two-dimensional model, conductivities around the cyclotron frequency region $\omega \sim 1$ are of the order of unity, $\sigma \sim 1$, which is an order of magnitude smaller than the DC conductivity found by Numata ($\sigma_{\mathrm{DC}} = 0.03^{-1} \approx 33$). Both of these values are less than the conductivity derived from combining Ampère's law with Ohm's law,

$$\sigma = \frac{\nabla \times \mathbf{B}}{\mu_0 \mathbf{E}}, \tag{3.12}$$

which in reduced units gives

$$\hat{\sigma} = \frac{1}{m_{\mathrm{A}}}. \tag{3.13}$$

where m_{A} is the Alfvén Mach number. In [2], Numata uses $m_{\mathrm{A}} = 0.01$. It is important to note that whereas Numata uses this method to estimate a

conductivity from a given electric field, Speiser in [22] uses this approach to find the allowable self-consistent electric field *given* a computed conductivity. From this it becomes clear that the Kubo conductivity, while negligible for small frequencies and DC values, can play a significant role when the electric field frequency is close to the cyclotron frequency.

It is clear that different formulations of the conductivity give different results. The Kubo-conductivity may not be well suited for calculating the DC-conductivity on systems where particles are known to escape quickly. The time spent outside the chaos region may also be problematic, as the bounce motion of a particle can be greatly affected by drift-velocity introduced by an applied electric field. In these situations the particle can leave the chaos region and not return. For this, a finite-lifetime model may be more appropriate. However, correlated motions over the entire region inside and outside the zone of chaos can become important for AC electric fields with frequencies on the order of the cyclotron frequency. The Kubo-conductivity is able to properly account for these motions, which makes it a powerful tool for computing AC conductivities.

The average dissipation $\langle \mathbf{j} \cdot \mathbf{E} \rangle$ can also be estimated, though the Kubo conductivity doesn't give any way to compute it directly. Here we consider the current as a sum of equilibrium and perturbation values,

$$\mathbf{j} = \mathbf{j}_0 + \delta\mathbf{j} = \mathbf{j}_0 + \sigma\delta\mathbf{E}. \tag{3.14}$$

For the two-dimensional system, the average equilibrium current in the z direction is governed by the grad-B drift. However, this drift has opposite directions for either side of the magnetic null line, which results in no average current for the equilibrium system. To calculate the perturbation dissipation D, we assume a periodic electric field,

$$D = \langle \mathbf{j} \cdot \mathbf{E}_0 \cos(\omega T) \rangle = \frac{\sum_i \sum_j \sigma_{ij}(\omega) E_{j0} E_{i0}}{2} = \frac{\sum_i \sum_j \rho_{ij}(\omega) j_j j_i}{2}, \tag{3.15}$$

where $i, j = x, y, z$ which is positive provided the conducitivty tensor is also positive. The above formula is valid for both systems with regular orbits and chaotic orbits. For regular systems, reversible dissipation is experienced only near the peaks around the cyclotron frequency ($\omega \sim \omega_{\mathrm{c}}$) and the bounce frequency ($\omega \sim \omega_{\mathrm{b}}$). For chaotic systems, irreversible dissipation will take place over a broad spectrum of frequencies, which the strongest dissipation occuring around and below the cyclotron frequency ($\omega \leq \omega_{\mathrm{c}}$).

Chapter 4

Three-dimensional null results

4.1 Magnetic field model

In this chapter the conductivity tensor $\sigma_{\mu\nu}(\omega)$ will be computed for the three-dimensional null systems considered in Parnell [3], as well as some quantitative properties of the regular orbits of the simpler potential null cases. The most general form of a linear magnetic field around a three-dimensional neutral point at the origin can be described using the form proposed in [3]

$$\mathbf{B} = \mathbf{M} \cdot \mathbf{r},$$

where $\mathbf{r}$ is the position vector and $\mathbf{M}$ is a 3×3 matrix of the form

$$\mathbf{M} = \begin{bmatrix} a_{11} & a_{12} & a_{13} \\ a_{21} & a_{22} & a_{23} \\ a_{31} & a_{32} & a_{33} \end{bmatrix},$$

where $a_{ij} = \partial B_i / \partial x_i$ are real constants. Using the divergence of the magnetic field, the trace of $\mathbf{M}$, along with its eigenvalues, sum to zero. This matrix can be reduced by exploiting certain properties of the linearized magnetic null.

Linear neutral points consists of two main features: a spine curve which approaches (or recedes from) a null point from two directions, and a fan surface which recedes (or approaches) the null point on a plane. As the eigenvalues sum to zero, one can be chosen to have a negative real part, while the other two can be chosen to have positive real parts. This set of eigenvalues describe positive neutral points where the spine curve points towards the origin.

Alternatively, a set with two eigenvalues with negative real parts describes a negative neutral point, where the spine diverges from the origin. Here we choose to examine positive neutral points. In this case the spine curve is described by the eigenvector of the negative eigenvalue, whereas the fan surface is described by a combination of the remaining two.

If the field lines in the fan plane expand in a radially symmetric way, then the null is called a *proper* radial null. If the field lines expand preferentially toward a specific vector in the fan plane, then the null is called an *improper* radial null [32] with minor and major fan axises. A null that contains logarithmic spirals in the fan plane is called a *proper* spiral null [33]. Finally, a null is called a critical spiral null [3] if the field lines curve in the fan plane, expanding asymptotically to straight lines without any preferential vector.

Here we chose the z-axis to lie along the direction of the spine curve. We can rotate this plane so the current perpendicular to the spine curve, $j_\perp$, lies on the x-axis. After dividing by a scaling factor, we formulate a simplified matrix M that is the sum of a potential (symmetric) matrix and a current (anti-symmetric) matrix,

$$\mathbf{M} = \begin{bmatrix} 1 & \frac{1}{2}(q - j_\parallel) & 0 \\ \frac{1}{2}(q + j_\parallel) & p & 0 \\ 0 & j_\perp & -(p+1) \end{bmatrix},$$

where p and q are potential parameters of the magnetic field and $j_\parallel$ is the current parallel to the spine curve. The eigenvalues of this matrix are

$$\lambda_1 = \frac{p + 1 + \sqrt{(p-1)^2 + q^2 - j_\parallel^2}}{2},$$
$$\lambda_2 = \frac{p + 1 - \sqrt{(p-1)^2 + q^2 - j_\parallel^2}}{2},$$
$$\lambda_3 = -(p+1).$$

To ensure that the z-axis corresponds to the spine curve (i.e. the third eigenvalue), $p \geq -1$ and $q^2 \leq j_\parallel^2 + 4p$. It will be useful to define a threshold

current

$$j_{\text{thresh}} = \sqrt{(p-1)^2 + q^2},$$

which reduces the eigenvalues to

$$\lambda_1 = \frac{p+1+\sqrt{j_{\text{thresh}}^2 - j_{\parallel}^2}}{2},$$
$$\lambda_2 = \frac{p+1-\sqrt{j_{\text{thresh}}^2 - j_{\parallel}^2}}{2},$$
$$\lambda_3 = -(p+1).$$

From this it is clear that the nature of the neutral point is determined by the relative size of j_{thresh} and $j_{\parallel}$. We shall deal with the current nulls in three cases, where $j_{\parallel}$ is less than, equal to, and great than j_{thresh}. When $j_{\perp} = 0$, we can do another rotation to eliminate q, giving

$$\mathbf{M} = \begin{bmatrix} 1 & -\frac{1}{2}j_{\parallel} & 0 \\ \frac{1}{2}j_{\parallel} & p & 0 \\ 0 & 0 & -(p+1) \end{bmatrix}.$$

It is worthwhile to note that when $p = 0$, the three dimensional neutral point devolves into a two-dimensional null line lying on the y-axis. As the parameter q has no effect on the overall topological structure of the linear magnetic null model, as well as an effect on the eigenvalues of $\mathbf{M}$, for simplicity we set $q = 0$ for all simulations.

4.1.1 Potential Nulls ($j_{\parallel} = j_{\perp} = 0$)

The initial simulations study the non-current magnetic field, also known as the potential null, i.e. $j_{\perp} = j_{\parallel} = q = 0$. Here,

$$\mathbf{M} = \begin{bmatrix} 1 & 0 & 0 \\ 0 & p & 0 \\ 0 & 0 & -(p+1) \end{bmatrix},$$

with eigenvalues $\lambda_1 = 1$, $\lambda_2 = p$, and $\lambda_3 = -(p+1)$ and $j_{\text{thresh}} = |p-1|$. In order for λ_3 to be associated with the spine curve, $p \geq 0$.

There are three main cases to consider for potential nulls. The first case, $j_{\text{thresh}} = 0$ and $p > 0$ deals with non-zero positive eigenvalues with two being equal. The next case, $j_{\text{thresh}}, p > 0$ deals with all non-zero and unequal eigenvalues. Finally, the third case is when one eigenvalue is zero, i.e. $p = 0$. It is useful to note that when $p > 1$, by dividing by $1/p$ and substituting for a new value, $p' = 1/p$, we see that

$$\mathbf{M} = \begin{bmatrix} p' & 0 & 0 \\ 0 & 1 & 0 \\ 0 & 0 & -(p'+1) \end{bmatrix},$$

which is identical to the case where $0 < p < 1$, but with the x and y axises interchanged. From this the only cases that need to be studied are for $0 \leq p \leq 1$. Here, we deal specifically with the values $p = 0, 0.1, 0.25, 0.5, 0.75$, and 1 to cover all three cases. In every case the spine is in the z direction while the fan plane is in the xy-plane. When $p = 1$, the null becomes a proper radial null, whereas when $0 < p < 1$ the null becomes an improper radial null. When $p = 0$, the null reduces to a two-dimensional null which consists of a series of X-points in xz-planes.

4.1.2 Current Nulls

Here $\mathbf{M}$ becomes antisymmetric and the magnetic field has a current of $\mathrm{J} = \left(j_\perp, 0, j_\parallel\right)$. The eigenvalues of $\mathbf{M}$ are

$$\lambda_{1,2} = \frac{1}{2}(p+1) \pm \frac{1}{2}\sqrt{j_{\text{thresh}}^2 - j_\parallel^2}, \quad \lambda_3 = -(p+1) \tag{4.1}$$

with $j_{\text{thresh}}^2 = (p-1)^2 + q^2$. To ensure that the eigenvector associated with λ_3 lies in the z-plane, $p \geq 1$ and $(p+1)^2 \geq j_{\text{thresh}}^2 - j_\parallel^2$.

$j_\parallel^2 < j_{\text{thresh}}^2$

The first case for the current null is when $j_\parallel^2 < j_{\text{thresh}}^2$, where all three eigenvalues are real and distinct, ensuring the existence of unique eigenvectors. This

can be divided into three further subcases where either $j_\parallel$ $j_\perp$ are non-zero or both are non-zero.

When only $j_\parallel$ is non-zero, the eigenvectors are

$$\mathbf{x}_{1,2} = \begin{pmatrix} \frac{1-p\pm\sqrt{j_{\text{thresh}}^2 - j_\parallel^2}}{j_\parallel} \\ 1 \\ 0 \end{pmatrix}, \quad \mathbf{x}_3 = \begin{pmatrix} 0 \\ 0 \\ 1 \end{pmatrix} \tag{4.2}$$

which forms an important null with field-lines expanding towards $\mathbf{x}_2$. In the case where $p = -j_\parallel^2/4$ the magnetic field becomes a two-dimensional null with X-points parallel to the plane $j_\parallel x - 2y = 0$ and a null line along $y = 2x/j_\parallel$.

When $j_\perp$ is non-zero, the eigenvectors become

$$\mathbf{x}_{1,2} = \begin{pmatrix} \frac{-3p^2+3+j_{\text{thresh}}^2 \pm 2(p+2)j_{\text{thresh}}}{2j_\perp\sqrt{j_{\text{thresh}}^2-(p-1)^2}} \\ \frac{3+3p\pm j_{\text{thresh}}}{2j_\perp} \\ 1 \end{pmatrix}, \quad \mathbf{x}_3 = \begin{pmatrix} 0 \\ 0 \\ 1 \end{pmatrix}, \tag{4.3}$$

where the plane of the fan is not perpendicular to the spine, but defined by the equation

$$2j_\perp\sqrt{j_{\text{thresh}}^2-(p-1)^2}x - 4j_\perp(p+2)y + \left[9(p+1)^2 - j_{\text{thresh}}^2\right]z = 0. \tag{4.4}$$

Here, the null is an improper null with field lines converging to the line

$$\mathrm{I}(\gamma) = \left(\frac{-3p^2+3+j_{\text{thresh}}^2+2(p+2)j_{\text{thresh}}}{2j_\perp\sqrt{j_{\text{thresh}}^2-(p-1)^2}}, \frac{3+3p+j_{\text{thresh}}}{2j_\perp}\gamma, \gamma\right). \tag{4.5}$$

When $p = j_{\text{thresh}} - 1$ the null becomes two-dimensional with X-points in the xz-plane and a null line

$$\mathrm{I}(\gamma) = \left(\frac{-(p+1)\sqrt{p}}{j_\perp}\gamma, \frac{p+1}{j_\perp}\gamma, \gamma\right). \tag{4.6}$$

Finally, when both $j_\perp$ and $j_\parallel$ are non-zero, the eigenvectors are

$$\mathbf{x}_{1,2} = \begin{pmatrix} \frac{-3p^2+3+j_{\text{thresh}}^2-j_\parallel^2 \pm 2(p+2)\sqrt{j_{\text{thresh}}^2-j_\parallel^2}}{2j_\perp\left(\sqrt{j_{\text{thresh}}^2-(p-1)^2}+j_\parallel\right)} \\ \frac{3(p+1)\pm\sqrt{j_{\text{thresh}}^2-j_\parallel^2}}{2j_\perp} \\ 1 \end{pmatrix}, \quad \mathbf{x}_3 = \begin{pmatrix} 0 \\ 0 \\ 1 \end{pmatrix}, \tag{4.7}$$

with fan plane

$$2j_\perp\left(\sqrt{j_{\text{thresh}}^2-(p-1)^2}+j_\parallel\right)x-4j_\perp(p+2)y+\left[9(p+1)^2-j_{\text{thresh}}^2+j_\parallel^2\right]z=0. \tag{4.8}$$

The null itself is an improper null with major fan axis x_1. When $(p+1)^2 = j_{\text{thresh}}^2 - j_\parallel^2$, the null becomes two-dimensional with X-points parallel to the plane

$$2px-\left(\sqrt{4p+j_\parallel^2}-j_\parallel\right)y=0 \tag{4.9}$$

with null line

$$\mathbf{I}(\gamma)=\left(\frac{-(p+1)\left(\sqrt{4p-j_\parallel^2}-j_\parallel\right)}{2j_\perp}\gamma,\frac{p_1}{j_\perp}\gamma,\gamma\right) \tag{4.10}$$

$j_\parallel^2 = j_{\text{thresh}}^2$

The eigenvalues for the case when $j_\parallel^2 = j_{\text{thresh}}^2$ are

$$\lambda_{1,2}=\frac{p+1}{2},\quad \lambda_3=-(p+1). \tag{4.11}$$

Since two eigenvalues are repeated, the uniqueness of three eigenvectors is no longer certain. Once again, this can be divided into three subcases where either $j_\parallel$ $j_\perp$ are non-zero or both are non-zero.

When $j_\perp$ is non-zero, the eigenvectors become

$$\mathbf{x}_1=\begin{pmatrix}1\\0\\0\end{pmatrix},\ \mathbf{x}_2=\begin{pmatrix}0\\\frac{3}{j_\perp}\\1\end{pmatrix},\ \mathbf{x}_3=\begin{pmatrix}0\\0\\1\end{pmatrix}, \tag{4.12}$$

with radial fan plane

$$j_\perp y-3z=0. \tag{4.13}$$

When $j_\parallel$ is non-zero, the two repeated eigenvalues have a single eigenvector. A Jordan basis vector $\mathbf{x}_2^*$ can be used as an extra vector to define the fan plane, which is found by solving the equation

$$\mathbf{M}\mathbf{x}_2^*=\lambda_1\mathbf{x}_2^*+\mathbf{x}_1 \tag{4.14}$$

where λ_1 is the repeated eigenvalue with eigenvector $\mathbf{x}_1$. The vectors used to define the fan plane and the spine are thus

$$\mathbf{x}_1 = \begin{pmatrix} \frac{1-p}{j_\parallel} \\ 1 \\ 0 \end{pmatrix}, \ \mathbf{x}_2^* = \begin{pmatrix} \frac{3-p}{j_\parallel} \\ 1 \\ 0 \end{pmatrix}, \ \mathbf{x}_3 = \begin{pmatrix} 0 \\ 0 \\ 1 \end{pmatrix}. \tag{4.15}$$

This results in a fan plane perpendicular to the spine with a critical spiral null. If $p = -1$, the plane $x = y$ becomes a neutral plane with anti-parallel field lines on either side.

When both $j_\perp$ and $j_\parallel$ are non-zero, the repeated eigenvector once again has only one associated eigenvector. After finding the Jordan basis vector, the vectors that describe the fan plane and the spine are

$$\mathbf{x}_1 = \begin{pmatrix} \frac{(3p^2-4p-11)\left(\sqrt{j_\parallel^2-(p-1)^2}-j_\parallel\right)}{2j_\perp(p-1)} \\ \frac{3(p+1)}{2j_\perp} \\ 0 \end{pmatrix},$$

$$\mathbf{x}_2^* = \begin{pmatrix} \frac{3(p+1)\left(\sqrt{j_\parallel^2-(p-1)^2}-j_\parallel\right)}{2j_\perp(p-1)^2} \\ \frac{3p+5}{2j_\perp} \\ 1 \end{pmatrix}, \ \mathbf{x}_3 = \begin{pmatrix} 0 \\ 0 \\ 1 \end{pmatrix}.$$

with fan plane

$$2j_\perp\left(\sqrt{j_\parallel^2-(p-1)^2}+j_\parallel\right)x - 4j_\perp(p+2)y + 9(p+1)^2 = 0. \tag{4.16}$$

A critical spiral is formed in the fan plane with major axis x_1. When $p = -1$, the z-axis becomes a null line with zero parabolic filed lines lying in parallel $x = y + c : z$-planes, where c is a constant.

$j_\parallel^2 > j_{\text{thresh}}^2$

In this case, $\lambda_1 = \bar{\lambda_2}$, where the overbar signifies the complex conjugate. This results in eigenvalues

$$\lambda_{1,2} = \frac{p+1}{2} \pm \frac{i}{2}\sqrt{j_\parallel^2 - j_{\text{thresh}}^2}, \lambda_3 = -(p+1). \tag{4.17}$$

As the eigenvectors of two complex conjugate eigenvalues are also complex conjugates, the fan plane will be defined seperately by the real and imaginary parts of these vectors. As $j_\parallel$ must be a positive non-zero number, the only case to consider is whether or not $j_\perp = 0$.

When $j_\perp$ is zero, the eigenvectors are

$$\mathbf{x}'_1 = \begin{pmatrix} \frac{1-p}{j_\parallel} \\ 1 \\ 0 \end{pmatrix}, \quad \mathbf{x}'_2 = \begin{pmatrix} \frac{\sqrt{j_\parallel^2 - j_{\text{thresh}}^2}}{j_\parallel} \\ 0 \\ 0 \end{pmatrix}, \quad \mathbf{x}_3 = \begin{pmatrix} 0 \\ 0 \\ 1 \end{pmatrix}. \tag{4.18}$$

with the fan plane being perpendicular to the spine, with spiral field lines of the form

$$\rho = \frac{C}{\sqrt{(p-1)\sin 2\phi + j_\parallel}} \tag{4.19}$$

$$\times \exp\left(\frac{(p+1)\tan^{-1}[(j_\parallel \tan\phi + p - 1)/\sqrt{j_\parallel^2 - (p-1)^2}]}{\sqrt{j_\parallel^2 - (p-1)^2}} \right) \tag{4.20}$$

where $\rho = \sqrt{x^2 + y^2}$, $\tan\phi = y/x$ and C is a constant. Logarithmic spirals occur when $p = 1$, where Eq. 4.19 reduces to

$$\rho = C \exp\left(\frac{2\phi}{j_\parallel}\right). \tag{4.21}$$

Field lines in this case oscillate around the spine until they arrive in the fan plane where they spiral out. When $p = -1$ the magnetic null becomes two-dimensional with a null line in the z-axis and concentric ellipses in planes parallel to the xy-plane.

When neither $j_\parallel$ or $j_\perp$ are zero, the eigenvectors are

$$\mathbf{x}'_1 = \begin{pmatrix} \frac{-3p^2+3+j_{\text{thresh}}^2 - j_\parallel^2}{2j_\perp\left(\sqrt{j_{\text{thresh}}^2 - (p-1)^2} + j_\parallel\right)} \\ \frac{3(p+1)}{2j_\perp} \\ 1 \end{pmatrix}, \tag{4.22}$$

$$\mathbf{x}'_2 = \begin{pmatrix} \frac{(p+2)\sqrt{j_\parallel^2 - j_{\text{thresh}}^2}}{j_\perp\left(\sqrt{j_{\text{thresh}}^2 - (p-1)^2} + j_\parallel\right)} \\ \frac{\sqrt{j_\parallel^2 - j_{\text{thresh}}^2}}{2j_\perp} \\ 0 \end{pmatrix}, \quad \mathbf{x}_3 = \begin{pmatrix} 0 \\ 0 \\ 1 \end{pmatrix}. \tag{4.23}$$

with the fan plane

$$2j_\perp\left(\sqrt{j_{\text{thresh}}^2-(p-1)^2}+j_\parallel\right)x-4j_\perp(p+2)y+(9(p+1)^2-j_{\text{thresh}}^2+j_\parallel^2)z=0. \tag{4.24}$$

Here, $p>-1$ to satisfy the λ_3-spine condition. When $p=-1$, the magnetic null once again becomes two-dimensional with a null line along the z-axis and elliptical field lines parallel to the plane

$$2j_\perp\left(\sqrt{j_{\text{thresh}}^2-4}+j_\parallel\right)x-4j_\perp y+(j_\parallel^2-j_{\text{thresh}}^2)z=0. \tag{4.25}$$

4.2 Regular dynamics

As with the two-dimensional null case, regular orbits of the three-dimensional null are those for which the adiabatic invariant μ is conserved. Typically these orbits occur at great distances away from the magnetic null. Regular dynamics for the three-dimensional potential null ($j_\perp = j_\parallel = 0$, $p \neq 0$) is characterized by two periodic motions around the null point, consistent of a bounce motion which oscillates between the spine and the fan plane, and a periodic ∇B motion with oscillates around the spine above the fan plane. The bounce motion can be calculated in a similar fashion[34] to Sec. 3.1. The field lines for the potential null are calculated by solving the differential equations

$$\frac{dx}{x}=\frac{dy}{py}=\frac{dz}{-(1+p)z} \tag{4.26}$$

which gives the solutions

$$y=c_1x^p \tag{4.27}$$

$$z=c_2x^{-(1+p)}, \tag{4.28}$$

where c_1 and c_2 are constants. The element of arc length along the field line is

$$ds^2=dx^2+dy^2+dz^2=dx^2\left(1+c_1^2p^2x^{2(p-1)}-c_2^2(1+p)^2x^{-2(2+p)}\right). \tag{4.29}$$

Once again, Eq. 3.5 is used to obtain the bounce frequency

$$f_{\mathrm{B}} = \frac{2}{v}\int_{x_1}^{x_2} \frac{\sqrt{1 + c_1^2 p^2 x^{2(p-1)} - c_2^2(1+p)^2 x^{-2(2+p)}}}{\sqrt{1 - \sin^2\theta_0 B_0^{-1}\sqrt{x^2 + c_1^2 p^2 x^{2p} + c_2^2(p+1)^2 x^{-2(p+1)}}}} dx. \quad (4.30)$$

where B_0 is the initial magnetic field and x_1, x_2. are the mirror points.

The precession frequency f_{p} can also be calculated by considering the average azimuthal velocity v_θ around the z-axis caused by the grad-B drift, as well as the curvature drift. Here we consider the potential null case. The combined grad-B and curvature drift is

$$\mathrm{v}_{\mathbf{R}+\nabla B} = \frac{m}{q}\left(v_\parallel^2 + \frac{1}{2}v_\perp^2\right)\frac{\mathbf{R}_{\mathrm{c}}\times\mathbf{B}}{R_{\mathrm{c}}^2 B^2} = \frac{m}{q}\left(v^2 - \mu B\right)\frac{\mathbf{R}_{\mathrm{c}}\times\mathbf{B}}{R_{\mathrm{c}}^2 B^2} \quad (4.31)$$

where μ is the first adiabatic invariant, $B = |\mathbf{B}|$ and $\mathbf{R}_{\mathrm{c}}$ is the radius of curvature, which is a vector of magnitude

$$R_{\mathrm{c}} = \frac{\left[1 + \left(\frac{df(x)}{dx}\right)^2\right]}{\left|\frac{d^2 f(x)}{dx^2}\right|} \quad (4.32)$$

which lies in the direction of curvature. Here, $f(x)$ is the function that defines a field line. The precession frequency f_{p} is calculated as

$$f_{\mathrm{p}} = 2\pi\left\langle v_\theta\right\rangle^{-1} = 2\pi\left(\frac{1}{s_2 - s_1}\int_{s_1}^{s_2}\mathrm{v}_\theta ds\right)^{-1}, \quad (4.33)$$

where s_1 and s_2 are the mirror points of the given field line. If the simplest case is considered, where a particle is confined to the xz-plane with $p = 1$, this becomes

$$\omega_{\mathrm{p}} = \frac{\mu}{q}\left(\frac{1}{t_2 - t_1}\int_{t_1}^{t_2}\frac{6zx}{(x^2 + 4z^2)^{3/2}}dt\right) \quad (4.34)$$

$$= \frac{\mu}{q}\left(\frac{1}{t_2 - t_1}\int_{t_1}^{t_2}\frac{6c_2 x(t)^{-1}}{(x(t)^2 + 4c_2^2 x(t)^{-4})^{3/2}}dt\right), \quad (4.35)$$

where x_1 and x_2 are the x mirror points of the given field line.

To verify the above equations, solutions are calculated using a particle with initial conditions $c_1 = 0$, $c_2 = 0.302$, $B_0 = 2.01$ and $\sin\theta_0 = 0.931$ and

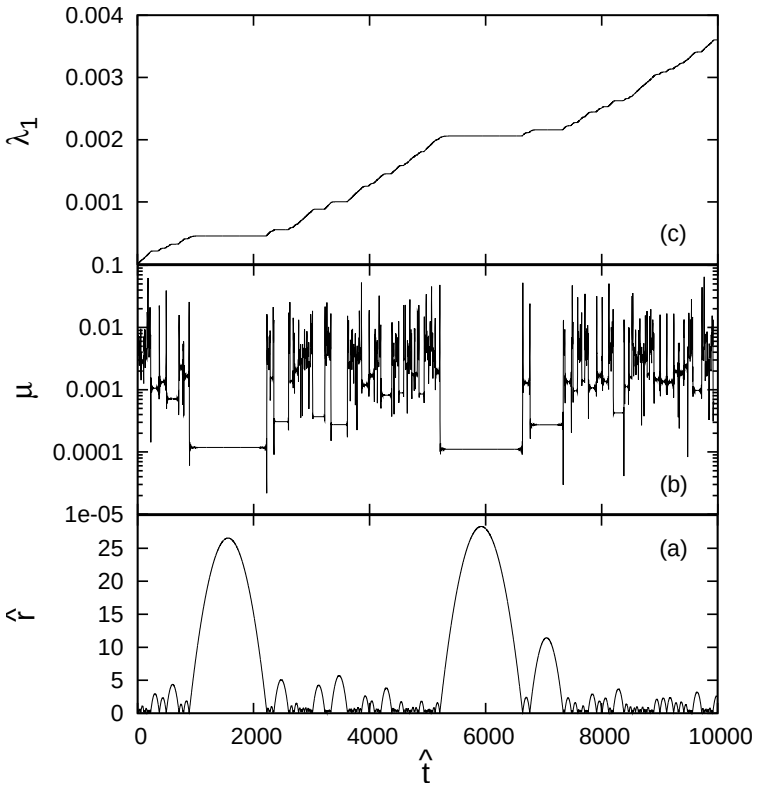

Figure 4.1: Results for a typical particle simulation for $p = 0.5$, $q = j_\perp = j_\parallel = 0$ versus time. (a) the distance from the origin. (b) evolution of the first adiabatic invariant μ. (c) $\lambda_1(t)$, normalized by the time of the simulation to give the maximal Lyapunov exponent.

calculated $x_1 = 0.5177$, $x_2 = 2.3129$, and $\mu = 2.01 \times 10^{-4}$. This gives a bounce frequency $f_\mathrm{b} = 2.60 \times 10^{-3}$ and a precession frequency of $f_\mathrm{p} = 1.1 \times 10^{-4}$. One needs to consider that these two motions form a product of cosines, so the bounce frequency peak actually becomes two peaks with lower and upper frequencies $\omega_{\mathrm{B},\pm} = \omega_\mathrm{B} \pm \omega_\mathrm{p}$. These agree with simulation results within an error of five percent.

4.3 Chaotic dynamics

Fig. 4.1 shows results for a typical particle trajection for $p = 0.5$, $q = j_\perp = j_\parallel = 0$ over the simulation. Fig. 4.1 a) shows the distance away from the magnetic null at the origin over time, while b) shows the first adiabatic invariant μ

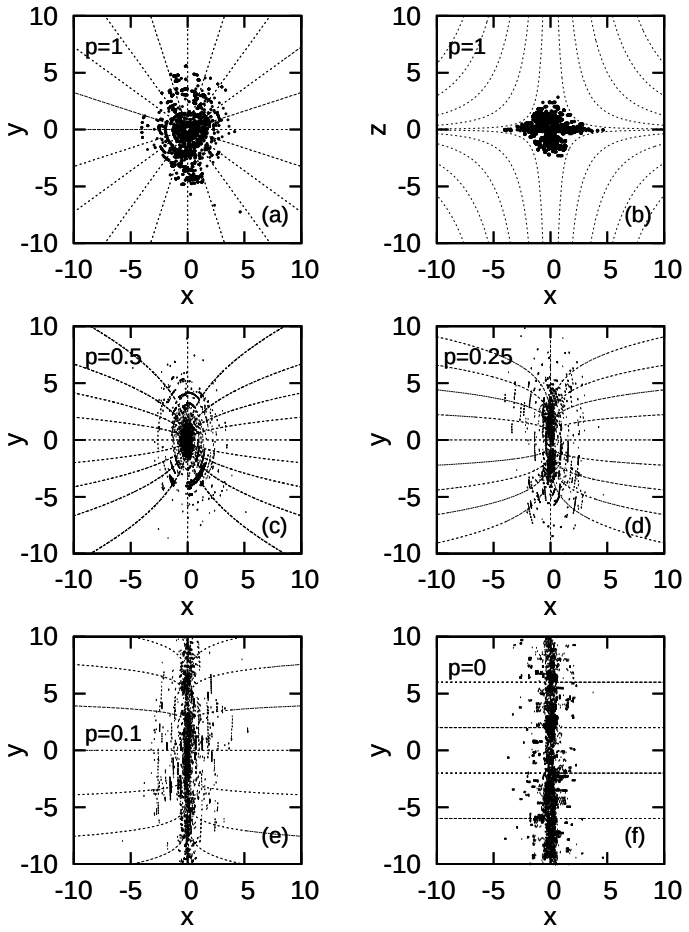

Figure 4.2: Chaotic particle trajectories for systems with varying values of p, $q = j_{\parallel} = j_{\perp} = 0$. Dashed lines indicate magnetic field lines. (a) and (b) are the x-y and x-z projections for $p = 1$, respectively. (c), (d), (e), (f) show the elongation of the chaos region in the y-direction for $p = 0.75, 0.5, 0.25$, and 0, respectively.

and c) shows $\lambda_1(t)$, scaled by the total time of the simulation. Far from the null the magnetic mirror force is directly proportional to μ which results in long parabolic orbits from the null if μ ever becomes sufficiently small. The growth of the Lyapunov exponent also ceases away from the null, while grows steadily near the null. It is clear that near the origin μ is not conserved and varies considerably. This results in travel times away from the null to vary sporadically in a non-deterministic way.

Fig. 4.2 shows the chaos region for potential nulls for p values of $1, 0.75, 0.5, 0.25$ and 0. Fig. 4.2(a) and (b) show the x-y and x-z projections

for the $p = 1$ system, respectively. The eigenvectors for potential nulls are the x,y, and z unit vectors, where the z unit vector corresponds to the spine and the x, y unit vectors correspond to the major and minor axes of the fan, respectively. The chaos region for this case can be best described as a sphere of unit radius, which reflects the azimuthal symmetry of the $p = 1$ system. This symmetry is broken for other values of p, as can be seen in the rest of the figures. For systems where $0 < p < 1$ the sphere becomes an ellipsoid with a unit minor radius and a major radius equal to p^{-1}. Here the minor axis of the ellipsoid lies along the major axis of the fan, while the minor axis of the ellipsoid lies along the major axis of the fan. The x-z projections of these systems are similar to that of the $p = 1$ case, and therefore are not shown in this diagram. For $p = 0$ the chaos region gives an infinitely long cylinder of unit radius as the y-direction is spatially symmetric.

Fig. 4.3 shows the chaos region for current nulls with $j_{\parallel}^2 < j_{\text{thresh}}^2$. The cases shown here are those studied in [3] which covers every specific case, as outlined in Sec. 4.1. A feature for the chaos regions for current nulls is that, as the field lines curve away from the fan axises, the structures that define the chaos region won't necessarily be described by the eigenvectors which define the magnetic null. The chaos zone in Fig. 4.3(a) can approximately be described as an ellipsoid with ordered radii $r_{1,2,3} = 7, 2, 1$ with r_1 lying in the direction $(1, 3.2, 0)$ and r_2 perpendicular to r_1 in the xy-plane. The degenerate case, Fig. 4.3(b), becomes an infinitely long cylinder with unit radius, oriented along the vector $(1, 2, 0)$. In the case where $j_{\parallel} = 0$, the chaos region in Fig. 4.3(c) can be described by an ellipsoid with ordered radii $r_{1,2,3} = 4, 1, 1$ with r_1 lying along the vector $(0, 1, 0.7)$. The degenerate case Fig. 4.3(d) becomes an infinitely long cylinder with unit radius that lies along the vector $(0, 1, -1)$. In the cases where both $j_{\parallel}$ and $j_{\perp}$ are non-zero, Fig. 4.3(e) and (f) show the xy and yz projections of the case where $p = 0.25$, $j_{\parallel} = 0.5$ and $j_{\perp} = 1$. The chaos

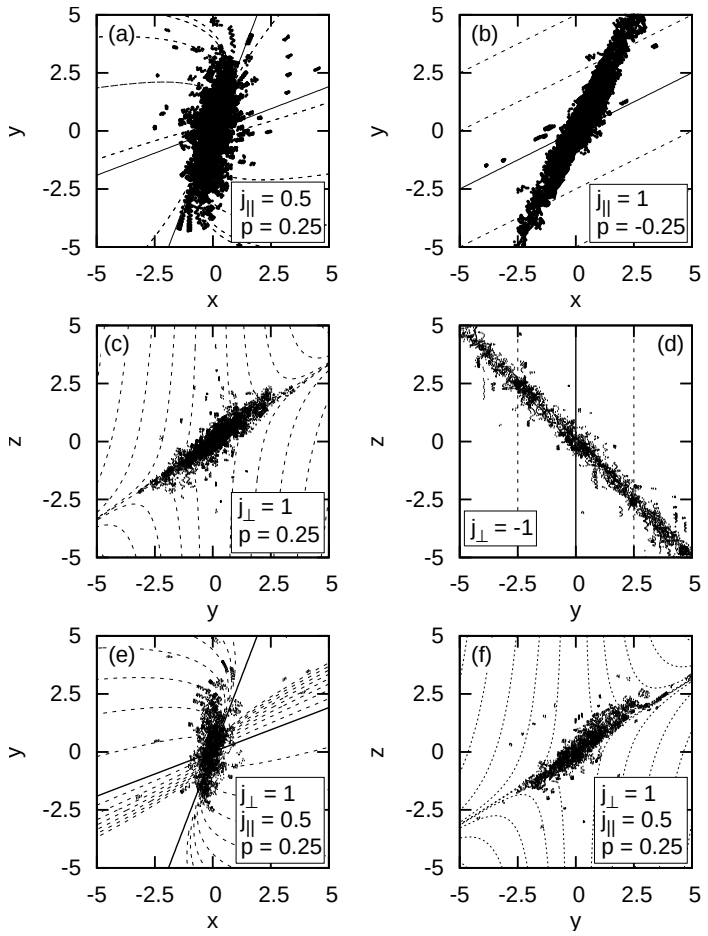

Figure 4.3: Chaotic particle trajectories for systems where $j_{\parallel}^2 < j_{\text{thresh}}^2$. Cases considered here are the cases studied in [3]. Dashed lines indicate magnetic field lines. Solid lines indicate fan axises and spine. For all systems, $q = 0$.

region can best be described as an ellipsoid of ordered radii $r_{1,2,3} = 7, 1, 1$ with r_1 along the vector (0.1,1,0.81). The degenerate case (not shown) is simply an infinitely long cylinder of unit radius along the vector (0.375,0.75,-1).

Fig. 4.4 shows the chaos region for magnetic nulls where $j_{\parallel}^2 = j_{\text{thresh}}^2$. The chaos zone for the region described in Fig. 4.4(a) is a simple sphere of unit radius on the origin. Fig. 4.4(b) shows a zone of chaos best described by an ellipsoid of ordered radii $r_{1,2,3} = 2, 1, 1$ with r_1 lying along the vector $(1, -1.67, 0)$. In the degenerate case, Fig. 4.4(c), the zone of chaos becomes an infinity long sheet of thickness $d = 2$, perpendicular to the vector $(1, -1, 0)$. Fig. 4.4(e) and (f) displays the general case when both $j_{\parallel}$ and $j_{\perp}$ are non-zero. This zone

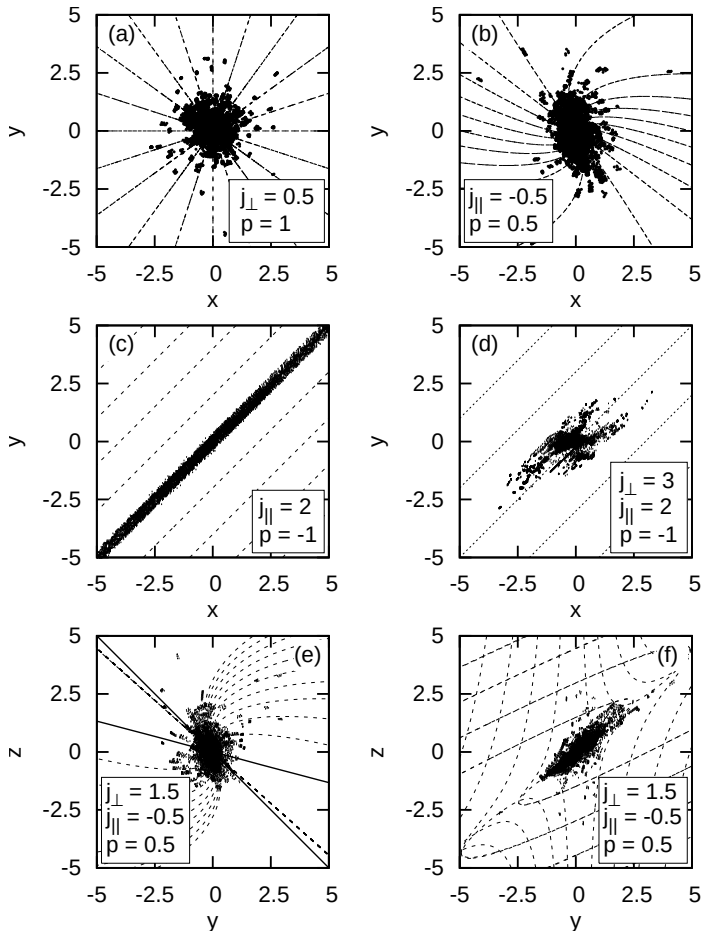

Figure 4.4: Chaotic particle trajectories for systems where $j_{\parallel}^2 = j_{\text{thresh}}^2$. Cases considered here are the cases studied in [3]. Dashed lines indicate magnetic field lines. Solid lines indicate fan axises and spine. For all systems, $q = 0$.

of chaos is desscribed as an ellipsoid with ordered radii $r_{1,2,3} = 3, 2, 1$ with r_1 lying along the vector $(-0.456, 1, 1)$. In the degenerate case,Fig. 4.4(d), the zone of chaos becomes an infinitely long cylinder with an ellipse base with radii $r_{1,2} = 3, 1$ with r_1 lying on the vector $(1, 0.75, 0)$.

Fig. 4.3 shows the chaos regions for magnetic nulls with $j_{\parallel}^2 > j_{\text{thresh}}^2$. The chaos region in Fig. 4.3(a) is best desribed as an ellipsoid of ordered radii $r_{1,2,3} = 2, 1, 1$ with r_1 lying along the vector $(1, 1.7, 0)$, while the chaos region in Fig. 4.3(b) can be described as an opoid with ordered radii $r_1 = 2, 1, 0.5$ with r_1 along $(2, 1, -1)$ and r_2 along the y axis. An ellipsoid also describes the null in Fig. 4.3(c) with ordered radii $r_{1,2,3} = 1, 1, 0.5$ with r_1 along $(-1, 1, 0)$ and

r_3 in along the z-axis. The degenerate case, Fig. 4.3(d) becomes an infinitely ellipse-based long cylinder on the z-axis with radii $r_{1,2} = 2, 1$ with r_1 along

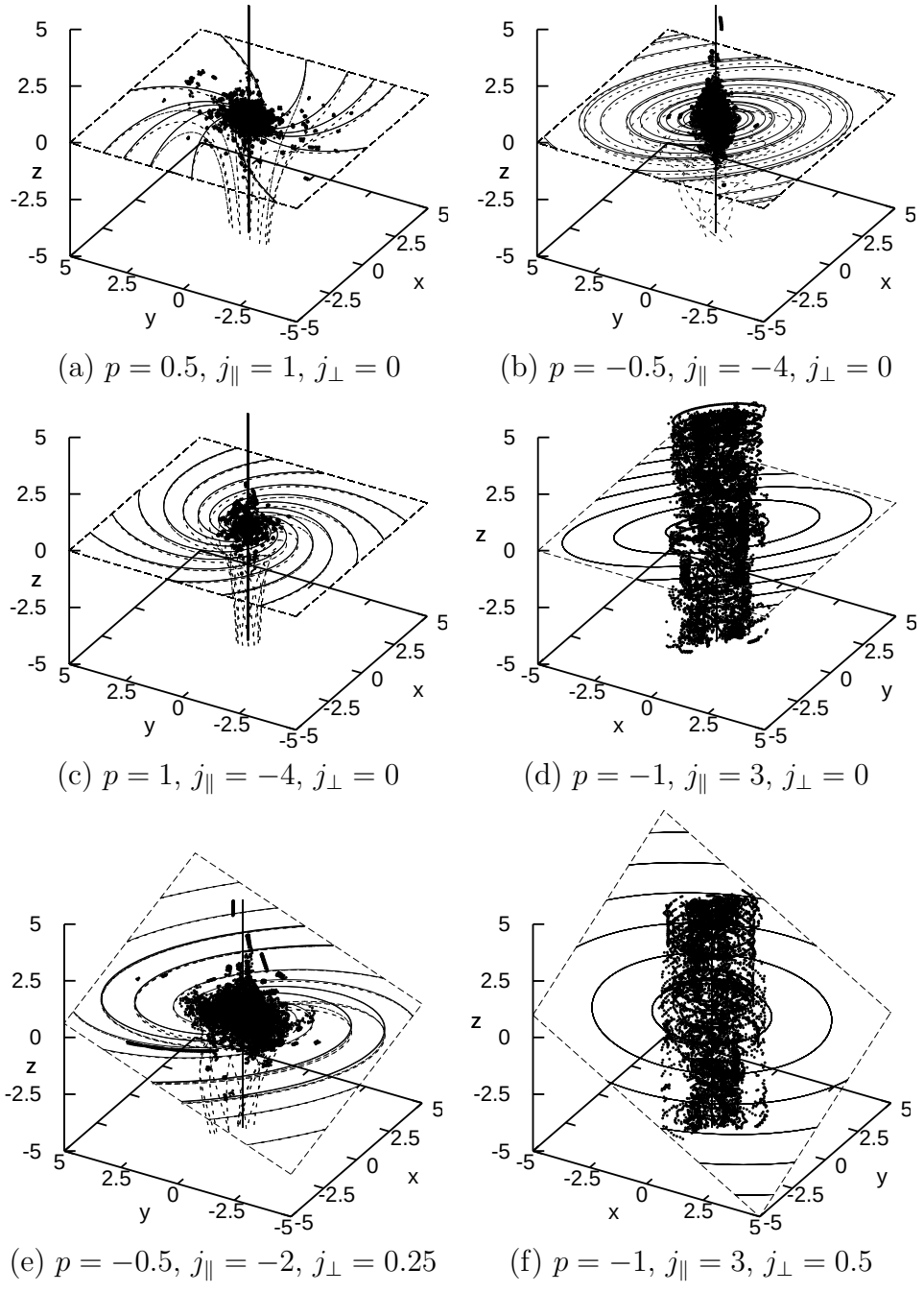

(a) $p = 0.5$, $j_\parallel = 1$, $j_\perp = 0$ (b) $p = -0.5$, $j_\parallel = -4$, $j_\perp = 0$

(c) $p = 1$, $j_\parallel = -4$, $j_\perp = 0$ (d) $p = -1$, $j_\parallel = 3$, $j_\perp = 0$

(e) $p = -0.5$, $j_\parallel = -2$, $j_\perp = 0.25$ (f) $p = -1$, $j_\parallel = 3$, $j_\perp = 0.5$

Figure 4.5: Regions of chaos for various systems where $j_\parallel^2 > j_{\text{thresh}}^2$. Solid lines signify fieldlines on the spine and fan plane whereas short-dashed lines signify fieldlines that run from the spine to the fan. Dots indicate points on particle trajectories that are considered chaotic. For all systems, $q = 0$.

the vector $(1, 1)$. Finally, for the cases where both $j_{\parallel}$ and $j_{\perp}$ are non-zero, the case in Fig. 4.3(e) can be described as an ellipse with ordered radii $r_{1,2,3} = 3, 0.8, 0.8$ with r_1 along $(-0.8, 1, 0.6)$. The chaos region for the degenerate case in Fig. 4.3(f) is described as an infinitely long ellipse-based cylinder on the $z - axis$ with radii $r_{1,2} = 2.5, 1$ with r_1 lying along the vector $(1, 1, 0)$.

Results from the calculation of the Lyapunov spectrum for all systems are tabulated in tab. 4.1. For all cases, the spectrum was computed using 2^{21} steps with a time step of $\Delta\hat{t} = 0.01$, averaged over 100 particles. As $\lambda_i = -\lambda_{6-i}$, and $\lambda_3 = \lambda_4 = 0$, only the first two Lyapunov exponents are shown. The maximal Lypunov exponents (MLE) ranges from the order of 10^{-2} to 10^{-4}, indicating that some systems are more chaotic than others. For the potential systems, the $p = 0$ system has the largest MLE, while the $p = 0.5$ system has the largest MLE for the three dimensional nulls. In general, the two-dimensional nulls have MLE larger than the three-dimenisonal nulls. The null plain system, where $p = -1$, $j_{\parallel} = 2$, and $j_{\perp} = q = 0$, contains the smallest set of Lyapunov exponents, indicating that it is the least chaotic of all systems studied here.

4.4 Conductivity results

Conductivity computations were carried out over 2^{21} time steps using 30000 particles with velocities drawn from a Maxwellian distribution with $v_{\mathrm{T}} = 0.05 v_{\mathrm{A}}$. Particles were positioned uniformly over their respective chaos regions as defined in sec. 4.3. For all cases, five runs with different initial conditions were computed to provide statistics for error analysis. Five additional runs over 2^{17}, 2^{18}, 2^{19} 2^{20}, and 2^{22} time steps were used to study the convergence of the conductivity tensor for every case. For all cases, $q = 0$.

p	$j_\parallel$	$j_\perp$	λ_1	λ_2
			Potential Nulls	
0	0	0	$(3.6 \pm 0.2) \times 10^{-2}$	$(8.6 \pm 5.4) \times 10^{-3}$
0.1	0	0	$(6.3 \pm 0.8) \times 10^{-3}$	$(4.9 \pm 0.6) \times 10^{-4}$
0.25	0	0	$(2.2 \pm 0.4) \times 10^{-2}$	$(3.8 \pm 2.1) \times 10^{-3}$
0.5	0	0	$(2.9 \pm 0.2) \times 10^{-2}$	$(6.5 \pm 0.5) \times 10^{-3}$
0.75	0	0	$(2.2 \pm 0.3) \times 10^{-2}$	$(3.6 \pm 3.3) \times 10^{-3}$
1	0	0	$(1.8 \pm 0.4) \times 10^{-2}$	$(1.2 \pm 0.6) \times 10^{-2}$
			$j_\parallel^2 < j_{\text{thresh}}^2$	
0.25	0.5	0	$(3.2 \pm 0.4) \times 10^{-3}$	$(3.8 \pm 0.6) \times 10^{-4}$
-0.25	1	0	$(1.9 \pm 0.2) \times 10^{-2}$	$(6.8 \pm 8.9) \times 10^{-7}$
0.25	0	1	$(6.4 \pm 0.5) \times 10^{-3}$	$(6.5 \pm 0.5) \times 10^{-4}$
0	0	-1	$(1.6 \pm 0.2) \times 10^{-2}$	$(2.6 \pm 0.2) \times 10^{-4}$
0.25	0.5	1	$(5.4 \pm 0.2) \times 10^{-3}$	$(6.0 \pm 0.6) \times 10^{-4}$
-0.25	1	-1	$(1.22 \pm 0.13) \times 10^{-2}$	$(2.56 \pm 0.10) \times 10^{-4}$
			$j_\parallel^2 = j_{\text{thresh}}^2$	
1	0	0.5	$(1.6 \pm 0.2) \times 10^{-2}$	$(5.2 \pm 0.6) \times 10^{-4}$
0.5	-0.5	0	$(6.1 \pm 0.6) \times 10^{-3}$	$(7.6 \pm 0.8) \times 10^{-4}$
-1	2	0	$(4.0 \pm 0.2) \times 10^{-4}$	$(1.7 \pm 0.2) \times 10^{-5}$
0.5	-0.5	1.5	$(6.1 \pm 0.6) \times 10^{-3}$	$(6.7 \pm 0.7) \times 10^{-4}$
-1	2	3	$(5.8 \pm 0.5) \times 10^{-3}$	$(3.7 \pm 0.2) \times 10^{-4}$
			$j_\parallel^2 > j_{\text{thresh}}^2$	
0.5	1	0	$(5.4 \pm 0.5) \times 10^{-3}$	$(7.1 \pm 0.7) \times 10^{-4}$
-0.5	-4	0	$(3.7 \pm 0.2) \times 10^{-3}$	$(1.08 \pm 0.07) \times 10^{-3}$
1	-4	0	$(8.9 \pm 1.3) \times 10^{-3}$	$(2.73 \pm 0.11) \times 10^{-4}$
-1	3	0	$(3.7 \pm 0.3) \times 10^{-2}$	$(3.30 \pm 0.10) \times 10^{-4}$
-0.5	-2	0.25	$(5.3 \pm 0.4) \times 10^{-3}$	$(8.4 \pm 0.6) \times 10^{-4}$
-1	3	0.5	$(1.35 \pm 0.15) \times 10^{-2}$	$(2.99 \pm 0.11) \times 10^{-4}$

Table 4.1: Lyapunov spectrum for all three-dimensional null systems of interest. As all systems considered are Hamiltonian, only the two unique non-zero Lyapunov exponents are tabulated. For all cases, $q = 0$.

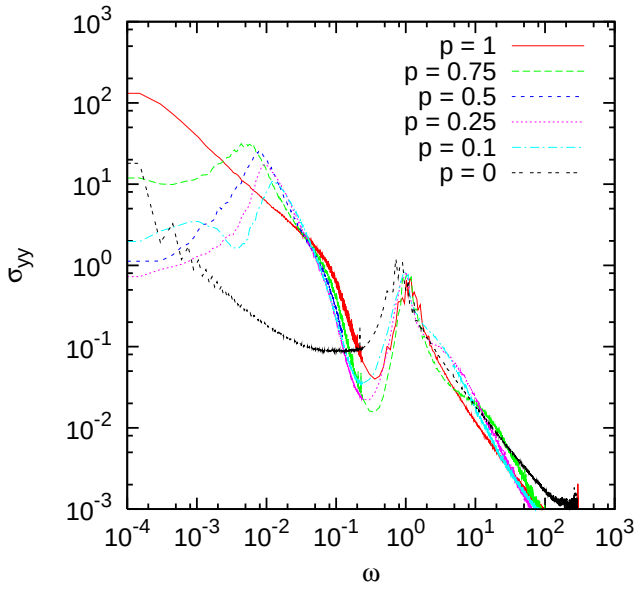

Figure 4.6: yy-component of the conductivity tensor $\sigma(\omega)$ for cases dealing with the potential magnetic null on a log-log scale. ω and σ_{yy} are in reduced units.

4.4.1 Potential Nulls

As the y component of the magnetic field is the most topologically dependent on the parameter p, the tensor component $\sigma_{yy}(\omega)$ will be considered first. Fig. 4.6 shows the yy compontent of the conducitivty tensor for all potential cases. Cyclotron motion produces peaks in all cases for frequencies around order unity, with the $p = 1$ case following a clear power-law ($\sigma_{\mu\nu}(\omega) = a_{\mu\nu}\omega^{b_{\mu\nu}}$) for all smaller frequencies. For all cases, the conductivity for frequences above the cyclotron region $\omega > 10$ becomes negligible. The $p = 0$ conductivity below the cyclotron frequency follows a power-law with an additional delta function which represents the average velocity in the y-direction, as seen in Sec. 3.3. The velocity is tabulated in Tab A.8. For intermediate cases where $0 < p < 1$, a distinct peak around $\omega = 10^{-2}$ is seen, with a decrease in conductivity for descreasing ω. However, as the simulation time is increased, theses peaks shift towards smaller ω as well as decrease in width. The power-law is thus computed from the points taken from the frequency region in between the

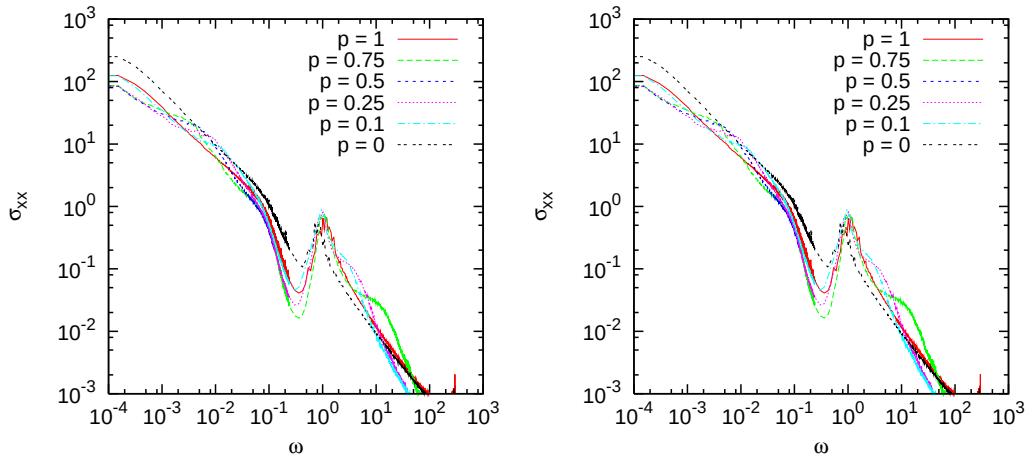

Figure 4.7: Conductivity tensor components $\sigma_{xx}(\omega)$ (a) and $\sigma_{zz}(\omega)$ (b) for potential null systems on a log-log scale. ω and σ_{xx} are in reduced units.

peak in question and the cyclotron frequency peak. All power law parameters are tabulated in Tab A.1.

Fig. 4.7 shows the conductivity tensor components $\sigma_{xx}(\omega)$ (a) and $\sigma_{zz}(\omega)$ on a log-log scale in reduced units using one run for each case. Below the cyclotron frequency $\omega_c \sim 1$, the conductivties follow decreasing power laws. For $\sigma_{xx}(\omega)$, cases $p = 0$ and $p = 1$ follow an overall similar shape, with the rest of the cases varying slightly. These differences becomes more pronounced for the $\sigma_{zz}(\omega)$. All power law parameters for the zz-conductivity tensor component are tabulated in Tab A.1. For all potential cases, off-diagonal tensor components are negligible, and are thus not plotted here.

4.4.2 Current Nulls

Fig. 4.8 shows the conductivity tensor components for (a) $\sigma_{xx}(\omega)$ and (b) $\sigma_{zz}(\omega)$ for the current nulls where $j_\parallel^2 < j_{\text{thresh}}^2$ with parameters $\left(p, j_\parallel, j_\perp\right)$. The conductivity curves are of similar shape to those in Fig. 4.7, with peaks around the cyclotron frequency $\omega_c \sim 1$ with addition to power laws below ω_B. For frequencies above the cyclotron frequency, $\omega > 10$, the conducivity becomes negligible.

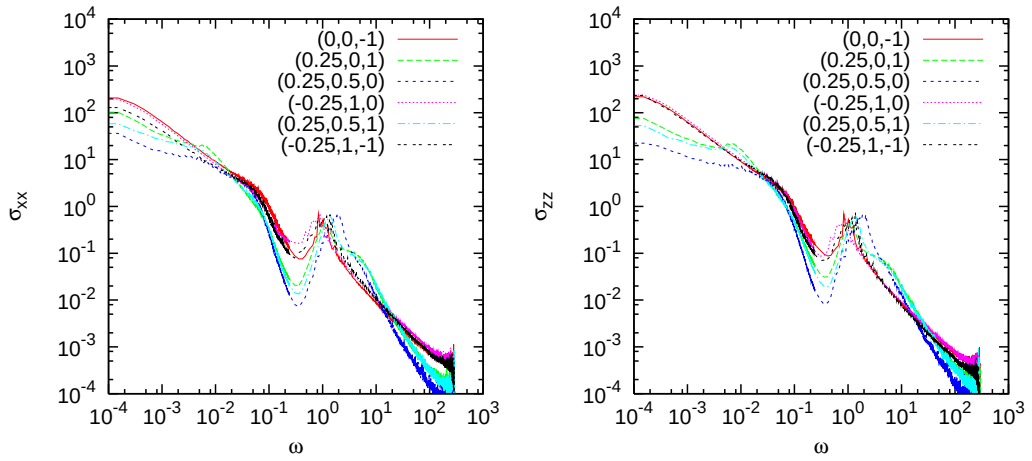

Figure 4.8: Conductivy tensor components $\sigma_{xx}(\omega)$ (a) and $\sigma_{zz}(\omega)$ (b) on a log-log scale for the current magnetic null with parameters $\left(p, j_{\parallel}, j_{\perp}\right)$ and $j_{\parallel}^2 < j_{\text{thresh}}^2$. ω and σ_{xx} are in reduced units.

Fig. 4.9 shows the yy-component of the conductivity tensor for the current null cases with $j_{\parallel}^2 < j_{\text{thresh}}^2$ with parameters $\left(p, j_{\parallel}, j_{\perp}\right)$. All cases show the characteric cyclotron peak around $\omega \sim 1$. The curves with parameters $(-0.25, 1, 0)$ and $(-0.25, 1, -1)$ follow clear powers for frequencies below the cyclotron frequency region $\omega < 10^{-1}$, with the $(0, 0, -1)$ following a power law with an additional delta function defined by a root mean squared velocity which is tabulated in Tab. A.8. Cases with $p = 0.25$ show a similar curve to the intermediate potential nulls as seen in Fig. 4.6. The peaks around $\omega \sim 10^{-2}$ move to smaller ω for larger time steps. In practice, the power law fit is calculated using points between this peak and the cyclotron region. The power law parameters for the diagonal conductivity tensor components of all potential nulls are tabulated in Tab. A.2.

Unlike the potential null systems, specific off-diagonal components for current nulls are not negligible. The case $(0, 0, -1)$ has a non-zero tensor component yz that is described by a power law with a negative prefactor. Power-laws with positive prefactors describe the xy tensor component for cases $(0.25, 0.5, 0)$, $(-0.25, 1, 0)$, $(-0.25, 1, -1)$, and $(0.25, 0.5, 1)$, with the two last

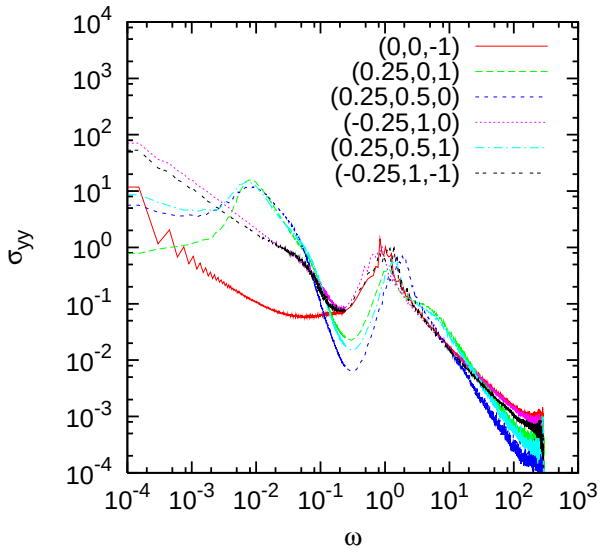

Figure 4.9: yy-component of the conductivity tensor $\sigma(\omega)$ for cases dealing with the current null for $j_\parallel^2 < j_{\text{thresh}}^2$ with parameters $\left(p, j_\parallel, j_\perp\right)$ on a log-log scale. ω and σ_{yy} are in reduced units.

cases also having non-zero xz and yz tensor components, also described by power laws. The case $(0.25, 0.5, 1)$ has an additional bulge in the yz tensor component which can be approximated by a Maxwellian peak with formed

$$\sigma(\omega) = \frac{a}{b^2}\omega^2 e^{-\omega^2/b^2}. \tag{4.36}$$

Finally, the case $(0.25, 0.5, 0)$ contains a Maxwellian peak near $\omega \approx 0.06$. All power-law parameters for non-diagonal tensor components are tabulated in Tab. A.5, while the Maxwellian curve parameters are tabulated in Tab. A.6.

Fig. 4.10 shows the conductivity tensor components (a) $\sigma_{xx}(\omega)$ and (b) $\sigma_{xx}(\omega)$ for current nulls with $j_\parallel^2 = j_{\text{thresh}}^2$ and parameters $\left(p, j_\parallel, j_\perp\right)$. As before, most curves show characteristic peaks around the cyclotron frequency $\omega_c \sim 1$, with the $(1, 0, 0.5)$ case following a power law for smaller frequencies. Instead of following a power-law, the $(-1, 2, 3)$ case is best described by the sum of a Maxwellian peak (Eq.4.36) and a translated Maxwellian peak with form

$$\sigma(\omega) = \frac{a}{b^2}(\omega - \omega_0)^2 e^{-(\omega-\omega_0)^2/b^2}. \tag{4.37}$$

In this case, the DC-value of the conductivity approaches the finite values

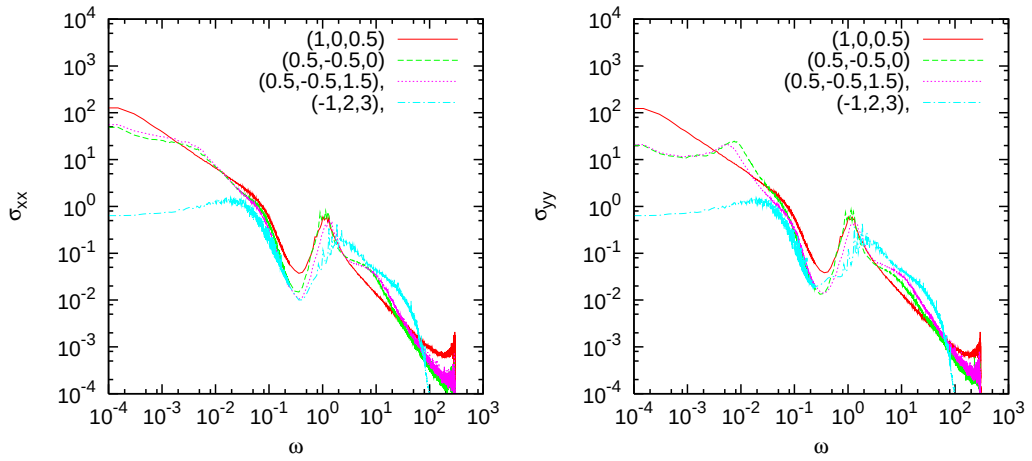

Figure 4.10: Conductivity tensor components $\sigma_{xx}(\omega)$ (a) and $\sigma_{yy}(\omega)$ (b) on a log-log scale for current nulls with $j_{\parallel}^2 = j_{\text{thresh}}^2$ and parameters $\left(p, j_{\parallel}, j_{\perp}\right)$. ω and σ_{xx} are in reduced units. The case $(-1, 2, 0)$ is not shown.

$\sigma_{xx,yy}(\omega = 0) = 0.667 \pm 0.004,\ 0.665 \pm 0.004$, respectively, with a slight increase for frequencies approaching the cyclotron region. This case decays faster than the other cases shown in Fig, 4.10. The parameters for this translated Maxwellian are tabulated in Tab. A.7, while parameters for the unshifted Maxwellian are presented in Tab. A.6.

Fig. 4.11 shows the conductivity tensor component $\sigma_{zz}(\omega)$ with $j_{\parallel}^2 = j_{\text{thresh}}^2$ and parameters $\left(p, j_{\parallel}, j_{\perp}\right)$. Most curves show characteristic cyclotron peaks as well as power laws below the cyclotron region $\omega < 10^{-1}$. The $(1, 2-3)$ case now follows a power-law,as well as an additional delta function with a mean squared velocity tabulate in Tab. A.8. As with the cases in Fig. 4.10, the $(-1, 2, 3)$ system decays faster than the other cases above the cyclotron frequency $\omega > 10$. The diagonal power-law parameters for the nulls with $j_{\parallel}^2 = j_{\text{thresh}}^2$ are tabulated in Tab. A.3.

As in the previous current null case, systems with $j_{\parallel}^2 = j_{\text{thresh}}^2$ have specific non-zero off-diagonal components of the conductivity tensor. Power-laws describe xy component for $(0.5, -0.5, 0)$, the yz component in $(0.5, -0.5, 0)$, and all components in $(0.5, -0.5, 1.5)$. Additional Maxwellian bulges appear in

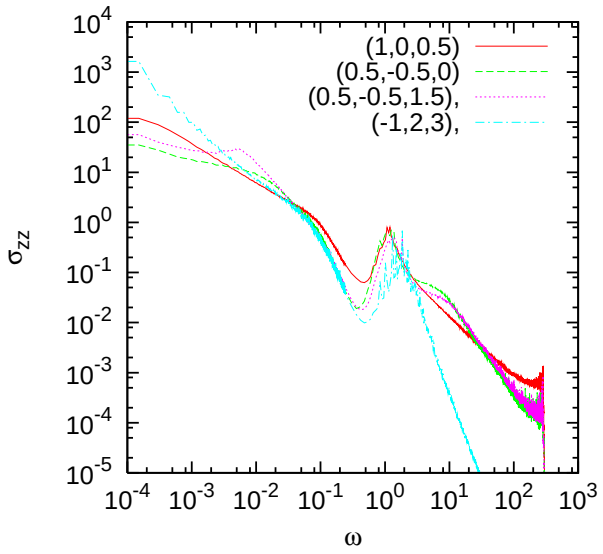

Figure 4.11: zz-component of the conductivity tensor $\sigma(\omega)$ for current nulls with $j_{\parallel}^2 = j_{\text{thresh}}^2$ and parameters $\left(p, j_{\parallel}, j_{\perp}\right)$ on a log-log scale. ω and σ_{yy} are in reduced units.

the xy component of $(0.5, -0.5, 0)$ and in the yz component of $(0.5, -0.5, 1.5)$. The xy component for the $(-1, 2, 3)$ closely follows the trend of the xx and yy diagonal components, consisting of a translated Maxwellian as well as an additional un-translated Maxwellian. Parameters for the off-diagonal power laws are tabulated in Tab. A.5. The parameters for the shifted and unshifted Maxwellian curves are tabulated in Tab. A.7 and Tab. A.6, respectively.

The current null case $(-1, 2, 0)$ has been omitted in both Fig. 4.10 and Fig. 4.11. As all field lines are parallel to the $z : x = y$-plane, with a drift velocity v_{D} in the z-direction, particles cannot leave the chaotic zone. However, while the adiabatic invariant μ may not be consered in this region, the particles tend to follow periodic orbits with drift velocity regardless. The Lyapunov exponent given in Tab. 4.1 is small enough for this system to be considered non-chaotic. The drift velocity, as well as the velocity along field lines, result in delta functions in all diagonal components of the conductivity tensor. The x-component of the field-line velocity is also directly correlated to the y-component of the field-line velocity, giving a delta function in the

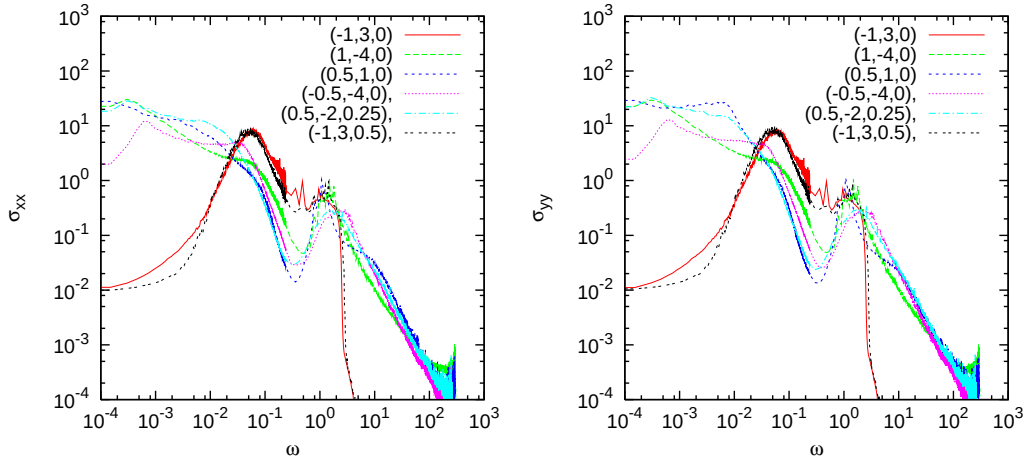

Figure 4.12: Conductivity tensor components $\sigma_{xx}(\omega)$ (a) and $\sigma_{yy}(\omega)$ (b) for current nulls with $j_\parallel^2 > j_{\text{thresh}}^2$ and parameters $\left(p, j_\parallel, j_\perp\right)$ on a log-log scale. ω and σ_{xx} are in reduced units.

xy components of the conductivity tensor. Delta functions also exist in the xz, yz components of the conductivity tensor, but are much less pronounced. All mean squared velocities are tabulated in Tab. A.8. Maxwellian peaks (Eq. 4.36) also appear around the cyclotron region $\omega_c \sim 1$ for all diagonal components of the conductivity tensor as well as the xy components. The parameters c_1 and $\Delta\omega$ are tabulated in Tab. A.6.

Fig. 4.12 shows the xx (a) and yy (b) conductivities for current nulls with $j_\parallel^2 > j_{\text{thresh}}$ and parameters on a $\left(p, j_\parallel, j_\perp\right)$ log-log scale. All cases show characteristic peaks near the cyclotron frequency $\omega_c \sim 1$. The cases $(1, -4, 0)$, $(0.5, 1, 0)$ and $(0.5, -2, 0.25)$ follow a power law for frequencies $\omega < 10^{-1}$. in both xx and yy conductivities, as well as the case $(0.5, 1, 0)$ in the yy, the conductivty has a slanted plateau in the frequency region $10^{-3} < \omega > 10^{-2}$, with a slight decrease for $\omega < 10^{-3}$. However, as the integration time of the simulations is increased, this plateau moves towards smaller frequencies along a line which would follow the power-law fit of the curve. This slanted plateau is subsequently ignored in the analysis of the numerical fits. Cases where $p = -1$ and $j_\parallel = 3$ show strong peaks around the cyclotron region $\omega \sim 1$ as well as an

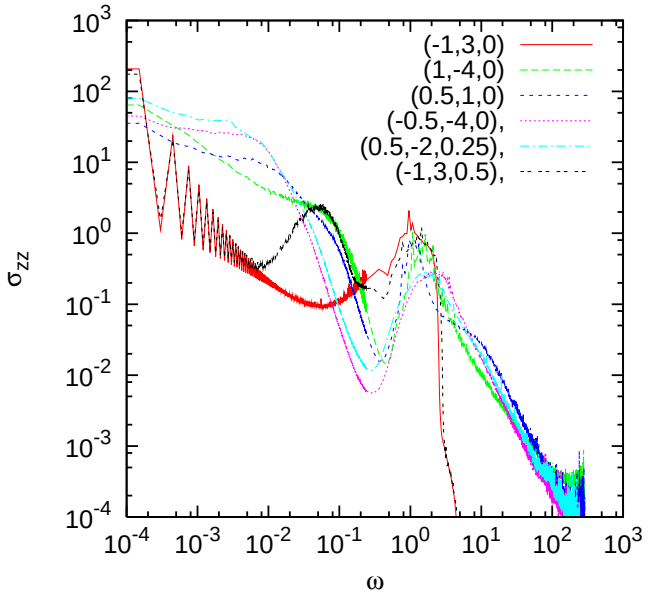

Figure 4.13: yy-component of the conductivity tensor $\sigma(\omega)$ for current nulls with $j_\parallel^2 > j_{\text{thresh}}^2$ and parameters $\left(p, j_\parallel, j_\perp\right)$ on a log-log scale. ω and σ_{yy} are in reduced units.

effection bounce frequency region $10^{-2} < \omega < 10^{-1}$ with tails on either side. These two curves appear to be the same for both cases. As the integration time of the simulations increases, these tails decrease in size, becoming negligible. Aside from the diminishing tail, both cases can be sufficiently described by the same two peaks. The two peaks themselves are very well approximated as the combination of two Maxwellian peaks with the form

$$\sigma(\omega) = \sum_i \frac{a_i}{b_i^2} \omega^2 e^{-\omega^2/b_i^2},$$

where a_i and b_i are fit parameters for either peak and $i = 1, 2$. These parameters are tabulated in Tab. A.6, while the rest of the power-law parameters are tabulated in Tab. A.4.

Fig. 4.13 shows the zz component of the conductivity tensor for current nulls with $j_\parallel^2 > j_{\text{thresh}}$ and parameters $\left(p, j_\parallel, j_\perp\right)$ on a log-log scale. The zz-component of the conductivity for the cases $(1, -4, 0)$, $(0.5, 1, 0)$ and $(0.5, -2, 0.25)$ evolves in a similar fashion to the xx and yy components of the conductivity. Cases where $p = -1$ and $j_\parallel = 3$ now include an additional power

law and delta function for frequencies below the cyclotron region $\omega < 10^{-2}$, with the $(-1, 3, 0.5)$ case only containing one Maxwellian peak around the cyclotron region $\omega \sim 1$. Maxwellian parameters are tabulated in Tab. A.6, while the rest of the power-law parameters are tabulated in Tab. A.4. The average square velocity for the delta function is tabulated in Tab. A.8.

Off-diagonal tensor components for the $j_{\parallel}^2 > j_{\text{thresh}}$ become slightly more complicated than the previous cases, with power laws appear in the xy components of $(-0.5, -4, 0)$, $(0.5, 1, 0)$ and $(-0.5, -2, 0.25)$. Maxwellian peaks feature more prominently in these tensor components, with two appearing in the xy component of $(-1, 3, 0)$, the xz component of $(-0.5, -2, 0.5)$, as well as all off-diagonal components of $(-1, 3, 0.5)$. The yz component of $(-0.5, -2, 0.25)$ actually contains three Maxwellian peaks, all well below the cyclotron region $\omega \sim 1$. Once again, power-law data for off-diagonal components are tabulated in Tab. A.5 while Maxwellian parameters are tabulated in Tab. A.6.

4.5 Discussion

Many interesting features arise from the Kubo conductivity when applied to three-dimensional magnetic nulls. As with the two-dimensional cases, the conductivities, with few exceptions, are generally well described by power laws. This reflects the fact that the Fourier transform of a power law t^α with exponent $-1 < \alpha < 0$ is also a power law with exponent $-(1 + \alpha)$. The velocity autocorrelations of chaotic orbits usually follow these types of power laws.

For many of these systems, the region around $\omega \sim 0, 2$ shows a noticeable decrease in conductivity. This inverted peak can be considered the region where both bounce frequency and cyclotron effects become negligible. As with the two-dimensional cases, for the three-dimensional nulls the conductivity is of order unity when the AC frequency is around the cyclotron region. In fact, throughout the entire range of frequency, the magnitude of the three-

dimensional conductivity (which match power-laws) is similar to that of the two-dimensional cases. This can be attributed to the total area underneath the conductivity, given by Eq. 2.28. Once again, the Kubo-conductivity becomes significant when dealing with electric perturbations with $\omega > \omega_c$.

The computation of the chaos zone reveals how varied systems behave depending on their topological properties. However, the chaos zone is generally localized to a region near the neutral structure (be it point, line, or plane), usually contained within a distance of order unity. The region of chaos is well defined for potential systems as an ellipsoid with major radius on the y-axis with magnitude proportional to p^{-1}. The Lyapunov spectrums for these systems, however, do not seem to follow any particular trend. As regions of chaos for the current nulls behave in a more complex manner, these cases must be dealt with individually, as no trend can be made between subcases. In general, the Lyapunov exponents for two-dimensional null systems are about a factor of $5-10$ larger than those for the three-dimensional case. However, the $(-1, 2, 3)$ case, which contains a null plane, has the smallest Lyapunov spectrum. Simulations of this case suggest a dominance of non-chaotic (adiabatic) trajectories.

While the Lyapunov spectrum gives insight on how chaotic a particular system may be, apart from non-chaotic systems, it bears no indication of the form of the conductivity tensor. It is clear that many of the three-dimensional null systems observe interesting conductivity curves that do not, in general, follow power laws. These cases are confined to the systems where $j_\parallel^2 \geq j_{\text{thresh}}^2$. The $(-1, 2, 3)$ case is of particular interest as this is the only case that exhibits a finite, non-zero value for the DC conductivity which converges for arbitrarily large integration times. The cases where $p = -1$ and $j_\parallel = 3$ also lack a power law for all tensor components (with the exception of zz), containing only Maxwellian peaks around a mean cyclotron frequency, as well as a mean

traversal frequency around O-shape field lines. These systems do not contain infinite field lines with increasing $|B|$, which result in an absence of bounce frequency mixing.

With the exception of a couple of cases, the appearance of off-diagonal components depends on the presence of B-field current. In order for the xy component of the conductivity tensor to be non-zero, $j_{\parallel}$ must be non-zero. Conversely, for there to exist a non-zero yz component of the conductivity tensor, $j_{\perp}$ must be non-zero. Finally, both $j_{\parallel}$ and $j_{\perp}$ must be non-zero for there to be a non-trivial yz component of the conductivity tensor. However, these conditions do not necessarily lead to non-zero off-diagonal components. The case $(1, -4, 0)$, while having a non-zero $j_{\parallel}$, has no non-trivial off-diagonal conductivity tensor components. The case $(-1, 2, 3)$ only has one non-trivial component of the conductivity tensor (xy), even though both $j_{\parallel}$ and $j_{\perp}$ are non-zero. While for most cases the sign of the current also matches the overall sign of the conductivity tensor component, this doesn't hold for every case. This shows that these systems must be studied on a case-by-case basis, due to the complex chaotic processes that are unique to each system.

Eq. 3.15 can be used to calculate the power dissipation of the three-dimensional null systems. Once again, as the current in reconnection system is the value most likely to be the primary variable, it may be advantageous to consider the resistive form of Eq. 3.15.

Chapter 5

Summary and Future Work

In this study, the complete Kubo-conductivity tensor for linear 2D and 3D magnetic nulls was computed using single particle simulations. The regions of chaos for each system were also determined through the use of Lyapunov exponents in order to provide a well-defined region in which to produce initial conditions. The conductivity tensor for the two-dimensional system proposed in Numata [2] was computed and compared against other conductivities, such as the Speiser conductivity. For these cases the diagonal components of the conductivity were well approximated by power-laws over the entire frequency range, with additional peaks in the cyclotron region. It was found that while the Kubo-conductivity resulted in negligible resistivity at low frequency, electric perturbations near the cyclotron frequency become significant and can be an order of magnitude larger than that derived from the Speiser formula. In these regions significant dissipation can occur from energy being carried away by accelerated particles. Off-diagonal components of the conductivity tensor for this system were found to be negligible.

The chaos regions for the three-dimensional potential null were found to be well-defined by an ellipsoid with major radius on the y-axis inversely proportional to the magnetic parameter p. Chaos regions for current nulls were found to be more complex, and had to be defined on a case-by-case basis.

The computation of the Lyapunov spectrum confirmed the stochasticity of most systems, with the exception of the case $(1, 2, 0)$ which was found to be non-chaotic.

Computation of the conductivity tensors for the three dimensional null systems show very complex behaviour between every case. For all cases, the value of the diagonal components of conductivity, in reduced units, is of order unity around the cyclotron frequency. The xx and zz components of the potential conductivity behave similarly between cases of varying p. The exponent of the yy-component of the conductivity between the $p = 0$ case and the $p = 0.1$ makes a jump to a higher value, while the prefactor decreases. As p is increased from $p = 0.1$ to $p = 1$, the prefactor of the power law increases as the exponent decreases. Current nulls display complex behaviour which necessitates the need to examine the conductivity tensor on a case-by-case basis. For off-diagonal components of the conductivity tensor to be non-negligible, certain requirements must be met, though satisfying these conditions is not sufficient to produce these conductivities.

The research presented in this thesis can be continued in a number of ways. Although comparisons have been made between DC conductivities, it would be worthwhile to compare AC-conductivities to real-world values, since around the cyclotron frequency the Kubo equation yields significant resistivities. Such alternating currents can be found in astrophysical plasmas as well a laboratory plasmas. More study can also be done with the three-dimensional null systems. In the potential null cases, the gap between the $p = 0$ case and the $p = 0.1$ can be studied further in order to see if there is any continuum in the yy-component of the conductivity. The computations of the three-dimensional current nulls performed in this study only consider a single instance of every subcase (specifically, the example systems given in Parnell [3]). Future studies can focus on specific subcases with multiple runs being performed to better

understand how the systems evolve with slight perturbations in the parameter space. Finally, a generalized form of the Kubo conductivity that includes the wavenumber term can be considered, which would broaden the potential real-applications of this method.

Bibliography

[1] C. J. Xiao. Cluster hits the magnetic bulls-eye, July 2006. URL `http://www.esa.int/esaSC/SEMAYXAUQPE_index_0.html`.

[2] R. Numata and Z. Yoshida. *Phys. Rev. Let.*, 88(4), 2002.

[3] C. E. Parnell, J. M. Smith, T. Neukirch, and E. R. Priest. *Phys. Plasmas*, 3:3, 1995.

[4] R. G. Giovanelli. *Mon. Not. R. Astron. Soc.*, 107:338, 1947.

[5] F. Holye. *Some Recent Researches in Solar Physics*. Cambridge University Press, New York, 1949.

[6] J. W. Dungey. *Philos. Mag.*, 7(44):725, 1953.

[7] C. J. Xiao, X. G. Wang, Z. Y. Pu, H. Zhao J. X. Wang, Z. W. Ma, S. Y. Fu, M. G. Kivelson, Z. X. Liu, Q. G. Zong, K. H. Glassmeier, A. Balogh, A. Korth, H. Reme11, and C. P. Escoubet. *Nat. Phys.*, 2:478, 2006.

[8] A. Stark, W. Fox, J. Egedal, O. Grulke, and T. Klinger. *Phys. Rev. Let.*, 95:235005, 2005.

[9] R. Fitzpartrick and T. C. Hender. *Phys. Fluids B*, 3(3):6445, 1991.

[10] R. Fitzpartrick. *Nuc. Fusion*, 33(7):1049, 1993.

[11] P. A. Sweet. *Electromagnetic Phenomena in Cosmical Physics*, page 123. Cambridge University Press, New York, 1958.

[12] E. N. Parker. *Astrophys. J. Suppl.*, (8):177, 1963.

[13] T. Yeh and W. I. Axford. *J. Plasma Phys.*, 4(2):207, 1970.

[14] H. E. Petschek. In *AAS-NASA symp. on Phys. of Solar Flares*, NASA SP-50, page 425, 1964.

[15] E. R. Priest and T. G. Forbes. *J. Geophys. Res.*, 91(A5):5579, 1986.

[16] M. Jardine and E. R. Priest. *J. Plasma Phys.*, 42(1):111, 1989.

[17] R. Kulsrud. *Earth Planets Space*, 53:417, 2001.

[18] H. Baty, E. R. Priest, and T. G. Forbes. *Phys. Plasmas*, 16:060701, 2009.

[19] R. K. Pathria. *Statistical Mechanics*. Eslevier Butterworth-Heinemann, second edition, 1996.

[20] F. Chen. *Plasma Physics and Controlled Fusion*. Springer, second edition, 1983.

[21] E. Priest and T. Forbes. *Magnetic Reconnection: MHD theory and applications*. Cambridge University Press, 2000.

[22] T. W. Speiser. *Planet Space Sci.*, 18:613, 1970.

[23] R. Kubo. *J. Phys. Soc. Japan*, 12(6):570, 1957.

[24] R. Kubo. *Rep. Prog. Phys.*, 29:255, 1966.

[25] W. Horton, C. Liu, B. Burns, and T. Tajima. *Phys. Fluids. B*, 3(8):2192, 1991.

[26] Jr R. F. Martin. *J. Geophys. Res.*, 91(A114):11,985, 1986.

[27] W. Horton and T. Tajima. *Geophys. Res. Let.*, 17(2):123, 1990.

[28] W. Horton and T. Tajima. *J. GeoPhys. Res.*, 96(A9):15811, 1991.

[29] D.L. Holland and J. Chen. *GeoPhys. Res. Let.*, 19(12):1231, 1992.

[30] S. W. H. Cowley. *Planet. Space Sci.*, 26, 1978.

[31] J. Hernandez, W. Horton, and T. Tajima. *J. GeoPhys. Res.*, 98(A4): 5893, 1993.

[32] S.W.H. Cowley. *Radio Sci.*, 8:903, 1973.

[33] S. Fukao, M. Ugai, and T. Tsuda. *Rep. Ion. Space Res. Jpn.*, 29:133, 1975.

[34] E. R. Priest and V. S. Titov. *Phil. Trans. R. Soc. Lond. A*, 354:2951–2992, 1996.

[35] C. E. Parnell and E. R. Priest. *Solar Phys.*, 151:57, 1994.

[36] E. R. Priest and D. I. Pontin. *Phys. Plasmas*, 16:122101, 2009.

[37] E. R. Priest and T. G. Forbes. *J. Geophys. Res.*, 97(A2):1521, 1992.

[38] H. X. Vu and J. U. Brackbill. *J. Comp. Phys.*, 116:384, 1995.

[39] A. Wolf, J. B. Swift, H. L. Swinney, and J. A. Vastano. *Physica*, 16(D): 285, 1984.

[40] I. Shimada and T. Nagashima. *Prog. of Theo. Phys.*, 61(6):1605, 1979.

[41] R. Courant and F. John. *Introduction to Calculus and Analysis*, volume II/1, chapter 2, pages 194–195. Springer, 1989.

[42] G. Benettin, L. Galgani, A. Giorgilli, and J.-M. Strelcyn. *Meccanica*, 15: 9, 1980.

[43] G. Benettin, L. Galgani, A. Giorgilli, and J.-M. Strelcyn. *Meccanica*, 15: 21, 1980.

Appendix A

Fit parameters

In this appendix the fit parameters for all functions mentioned in Chapter 4 are tabulated, along with any given errors. All functions are fit using the method of non-linear least squares. Errors are generated by calculating the standard error of the mean (denoted by SE), given by

$$\mathrm{SE} = \frac{\sigma}{\sqrt{n}}$$

where n is the number of samples and σ is the sample standard deviation. For all cases, five samples are used. While errors are given for prefactors for the fitting functions, it is expected that these values are to be used as an order of magnitude estimate.

Power laws were fitted over a small frequency range of the conductivity curves. The ranges were determined by running simulations with varying total simulation time and noting the range over which conductivity curves converged to a power law. The range of the power law would increase with the total time of the simulation. Care was taken to ensure that points for which frequencies would be undersampled were not included in these fits. Undersampled points are those beyond the Nyquist frequency ($\omega_{\mathrm{max}} = \pi/\Delta t$) and those below the Nyquist rate ($\omega_{\mathrm{min}} = \pi/N\Delta t$), where Δt is the timestep, N is the total number of steps, and $\omega_{\mathrm{max,min}}$ is the upper and lower bound of properly sampled frequencies, respectively. In practice, frequencies within a factor of

two of these bounds are also considered undersampled.

p	a_{xx}	b_{yy}
0	0.182 ± 0.002	-0.861 ± 0.002
0.1	0.342 ± 0.004	-0.661 ± 0.003
0.25	0.754 ± 0.008	-0.509 ± 0.004
0.5	0.377 ± 0.006	-0.637 ± 0.003
0.75	0.351 ± 0.06	-0.654 ± 0.003
1	0.173 ± 0.002	-0.774 ± 0.002
p	a_{yy}	b_{yy}
0	$(8.82 \pm 0.05) \times 10^{-3}$	-0.650 ± 0.003
0.1	$(5.98 \pm 0.15) \times 10^{-3}$	-1.810 ± 0.009
0.25	$(5.94 \pm 0.10) \times 10^{-3}$	-1.785 ± 0.005
0.5	$(9.10 \pm 0.11) \times 10^{-3}$	-1.654 ± 0.003
0.75	$(1.93 \pm 0.10) \times 10^{-2}$	-1.423 ± 0.003
1	0.173 ± 0.005	-0.775 ± 0.002
p	a_{zz}	b_{zz}
0	0.181 ± 0.003	-0.861 ± 0.002
0.1	0.270 ± 0.013	-0.689 ± 0.009
0.25	0.754 ± 0.007	-0.509 ± 0.002
0.5	0.876 ± 0.004	-0.459 ± 0.002
0.75	0.829 ± 0.011	-0.479 ± 0.03
1	0.131 ± 0.003	-0.808 ± 0.005

Table A.1: Parameters for the potential null power laws.

$(p, j_\parallel, j_\perp)$	a_{xx}	b_{yy}
$(0, 0, -1)$	0.219 ± 0.002	-0.818 ± 0.002
$(0.25, 0, 1)$	0.431 ± 0.003	-0.644 ± 0.002
$(0.25, 0.5, 0)$	0.665 ± 0.02	-0.482 ± 0.005
$(-0.25, 1, 0)$	0.181 ± 0.002	-0.823 ± 0.002
$(-0.25, 1, -1)$	0.255 ± 0.002	-0.723 ± 0.002
$(0.25, 0.5, 1)$	0.595 ± 0.005	-0.555 ± 0.002
$(p, j_\parallel, j_\perp)$	a_{yy}	b_{yy}
$(0, 0, -1)$	$(5.03 \pm 0.09) \times 10^{-3}$	-0.660 ± 0.002
$(0.25, 0, 1)$	$(6.53 \pm 0.02) \times 10^{-3}$	-1.677 ± 0.009
$(0.25, 0.5, 0)$	$(3.02 \pm 0.07) \times 10^{-2}$	-1.327 ± 0.006
$(-0.25, 1, 0)$	$(4.64 \pm 0.05) \times 10^{-2}$	-0.834 ± 0.002
$(-0.25, 1, -1)$	$(6.62 \pm 0.06) \times 10^{-2}$	-0.725 ± 0.002
$(0.25, 0.5, 1)$	$(1.72 \pm 0.03) \times 10^{-2}$	-1.411 ± 0.005
$(p, j_\parallel, j_\perp)$	a_{zz}	b_{zz}
$(0, 0, -1)$	0.216 ± 0.003	-0.820 ± 0.003
$(0.25, 0, 1)$	0.699 ± 0.005	-0.553 ± 0.002
$(0.25, 0.5, 0)$	1.30 ± 0.03	-0.331 ± 0.005
$(-0.25, 1, 0)$	0.253 ± 0.003	-0.805 ± 0.002
$(-0.25, 1, -1)$	0.293 ± 0.002	-0.762 ± 0.02
$(0.25, 0.5, 1)$	1.03 ± 0.07	-0.468 ± 0.005

Table A.2: Parameters for the current null power laws where $j_\parallel^2 < j_{\text{thresh}}^2$.

$(p, j_\parallel, j_\perp)$	a_{xx}	b_{yy}
$(1, 0, 0.5)$	0.157 ± 0.004	-0.803 ± 0.003
$(0.5, -0.5, 0)$	0.505 ± 0.008	-0.562 ± 0.004
$(0.5, -0.5, 1.5)$	0.476 ± 0.005	-0.597 ± 0.002
$(p, j_\parallel, j_\perp)$	a_{yy}	b_{yy}
$(1, 0, 0.5)$	0.152 ± 0.003	-0.810 ± 0.007
$(0.5, -0.5, 0)$	$(1.20 \pm 0.02) \times 10^{-3}$	-1.57 ± 0.03
$(0.5, -0.5, 1.5)$	$0.936 \pm 0.005) \times 10^{-3}$	-0.426 ± 0.003
$(p, j_\parallel, j_\perp)$	a_{zz}	b_{zz}
$(1, 0, 0.5)$	0.198 ± 0.002	-0.751 ± 0.002
$(0.5, -0.5, 0)$	0.927 ± 0.011	-0.437 ± 0.003
$(0.5, -0.5, 1.5)$	1.240 ± 0.011	-0.475 ± 0.008
$(-1, 2, 3)$	$(3.40 \pm 0.09) \times 10^{-2}$	-1.15 ± 0.02

Table A.3: Parameters for the current null power laws where $j_\parallel^2 = j_{\text{thresh}}^2$

$(p, j_\parallel, j_\perp)$	a_{xx}	b_{yy}
$(0.5, 1, 0)$	0.759 ± 0.002	-0.435 ± 0.005
$(-0.5, 4, 0)$	0.510 ± 0.002	-0.427 ± 0.003
$(1, -4, 0)$	0.258 ± 0.003	-0.584 ± 0.003
$(-0.5, -2, 0.25)$	1.19 ± 0.03	-0.410 ± 0.005
$(p, j_\parallel, j_\perp)$	a_{yy}	b_{yy}
$(0.5, 1, 0)$	$(2.87 \pm 0.02) \times 10^{-2}$	-1.34 ± 0.05
$(-0.5, 4, 0)$	0.481 ± 0.002	-0.448 ± 0.002
$(1, -4, 0)$	0.257 ± 0.003	-0.584 ± 0.003
$(-0.5, -2, 0.25)$	$(0.923 \pm 0.018) \times 10^{-2}$	-0.470 ± 0.005
$(p, j_\parallel, j_\perp)$	a_{zz}	b_{zz}
$(0.5, 1, 0)$	$(7.06 \pm 0.06) \times 10^{-2}$	-1.06 ± 0.02
$(-0.5, 4, 0)$	1.419 ± 0.013	-0.443 ± 0.002
$(-1, 3, 0)$	$(1.89 \pm 0.03) \times 10^{-2}$	-0.507 ± 0.002
$(1, -4, 0)$	0.207 ± 0.004	-0.659 ± 0.004
$(-0.5, -2, 0.25)$	4.09 ± 0.02	-0.339 ± 0.003
$(-1, 3, 0.5)$	$(8.81 \pm 0.07) \times 10^{-3}$	-0.641 ± 0.003

Table A.4: Parameters for the current null power laws where $j_\parallel^2 > j_{\text{thresh}}^2$

$(p, j_\parallel, j_\perp)_{\mu\nu}$	$a_{\mu\nu}$	$b_{\mu\nu}$
	$j_\parallel^2 < j_{\text{thresh}}^2$	
$(0, 0, -1)_{yz}$	$(-1.6 \pm 0.3) \times 10^{-4}$	-1.15 ± 0.04
$(0.25, 0.5, 0)_{xy}$	$(5.54 \pm 0.08) \times 10^{-2}$	-0.62 ± 0.004
$(-0.25, 1, 0)_{xy}$	$(8.23 \pm 0.02) \times 10^{-2}$	-0.843 ± 0.003
$(-0.25, 1, -1)_{xy}$	0.138 ± 0.002	-0.709 ± 0.003
$(-0.25, 1, -1)_{xz}$	$(-2.95 \pm 0.05) \times 10^{-2}$	-0.870 ± 0.003
$(-0.25, 1, -1)_{yz}$	$(-6.68 \pm 0.03) \times 10^{-3}$	-1.012 ± 0.009
$(0.25, 0.5, 1)_{xy}$	$(1.67 \pm 0.05) \times 10^{-2}$	-0.833 ± 0.005
$(0.25, 0.5, 1)_{xz}$	$(1.31 \pm 0.05) \times 10^{-2}$	-0.799 ± 0.009
$(0.25, 0.5, 1)_{yz}$	$(2.01 \pm 0.05) \times 10^{-2}$	-0.652 ± 0.004
	$j_\parallel^2 = j_{\text{thresh}}^2$	
$(1, 0, 0.5)_{yz}$	$(6.92 \pm 0.02) \times 10^{-2}$	-0.668 ± 0.004
$(0.5, -0.5, 0)_{xy}$	$(-3.04 \pm 0.07) \times 10^{-2}$	-0.789 ± 0.003
$(0.5, -0.5, 1.5)_{xy}$	$(-4.28 \pm 0.08) \times 10^{-2}$	-0.770 ± 0.002
$(0.5, -0.5, 1.5)_{xz}$	$(-2.32 \pm 0.10) \times 10^{-2}$	-0.778 ± 0.017
$(0.5, -0.5, 1.5)_{yz}$	$(6.36 \pm 0.11) \times 10^{-2}$	-0.646 ± 0.003
	$j_\parallel^2 > j_{\text{thresh}}^2$	
$(-0.5, -4, 0)_{xy}$	0.110 ± 0.008	-0.398 ± 0.017
$(0.5, 1, 0)_{xy}$	$(2.1 \pm 0.6) \times 10^{-2}$	-0.70 ± 0.03
$(-0.5, -2, 0.25)_{xy}$	-0.358 ± 0.008	-0.499 ± 0.006

Table A.5: Parameters for all off-diagonal power law fits for current nulls.

$(p, j_\parallel, j_\perp)_{\mu\nu}$	$a_{\mu\nu}$	$b_{\mu\nu}$
	$j_\parallel^2 < j_{\text{thresh}}^2$	
$(0.25, 0, 1)_{yz}$	$(3.38 \pm 0.02) \times 10^{-4}$	$(6.60 \pm 0.04) \times 10^{-2}$
$(0.25, 0.5, 1)_{yz}$	22.5 ± 0.3	$(7.47 \pm 0.04) \times 10^{-2}$
	$j_\parallel^2 = j_{\text{thresh}}^2$	
$(0.5, -0.5, 0)_{xy}$	-20.5 ± 0.4	$(3.50 \pm 0.06) \times 10^{-3}$
$(-1, 2, 0)_{xx}$	3.42 ± 0.11	0.509 ± 0.010
$(-1, 2, 0)_{xy}$	-3.36 ± 0.11	0.508 ± 0.010
$(-1, 2, 0)_{yy}$	3.42 ± 0.011	0.509 ± 0.010
$(-1, 2, 0)_{zz}$	2.30 ± 0.13	0.832 ± 0.003
$(0.5, -0.5, 1.5)_{yz}$	40.5 ± 0.4	$(5.66 \pm 0.03) \times 10^{-3}$
$(-1, 2, 3)_{xx}$	0.628 ± 0.010	2.54 ± 0.05
$(-1, 2, 3)_{xy}$	-0.140 ± 0.007	2.11 ± 0.03
$(-1, 2, 3)_{yy}$	0.614 ± 0.010	2.58 ± 0.03
$(-1, 2, 3)_{zz}$	-0.382 ± 0.011	0.215 ± 0.009
	$j_\parallel^2 > j_{\text{thresh}}^2$	
$(-1, 3, 0)_{xx1}$	21.0 ± 0.04	$(6.69 \pm 0.02) \times 10^{-2}$
$(-1, 3, 0)_{xx2}$	1.49 ± 0.02	1.11 ± 0.03
$(-1, 3, 0)_{xy1}$	9.55 ± 0.05	$(7.16 \pm 0.03) \times 10^{-2}$
$(-1, 3, 0)_{xy2}$	-0.590 ± 0.007	1.485 ± 0.009
$(-1, 3, 0)_{yy1}$	21.0 ± 0.04	$(6.69 \pm 0.02) \times 10^{-2}$
$(-1, 3, 0)_{yy2}$	1.48 ± 0.03	1.113 ± 0.005
$(-1, 3, 0)_{zz}$	1.48 ± 0.03	1.123 ± 0.005
$(0.5, 1, 0)_{xy}$	3.00 ± 0.03	$(3.84 \pm 0.04) \times 10^{-3}$
$(-0.5, -2, 0.25)_{xz1}$	5.8 ± 0.2	$(1.40 \pm 0.03) \times 10^{-3}$
$(-0.5, -2, 0.25)_{xz2}$	1.91 ± 0.03	$(1.11 \pm 0.03) \times 10^{-2}$
$(-0.5, -2, 0.25)_{yz1}$	26.3 ± 1.0	$(3.89 \pm 0.02) \times 10^{-4}$
$(-0.5, -2, 0.25)_{yz2}$	15.1 ± 0.2	$(2.51 \pm 0.02) \times 10^{-3}$
$(-0.5, -2, 0.25)_{yz3}$	10.1 ± 0.3	$(8.56 \pm 0.05) \times 10^{-3}$
$(-1, 3, 0.5)_{xx1}$	21.0 ± 0.07	$(5.80 \pm 0.02) \times 10^{-2}$
$(-1, 3, 0.5)_{xx2}$	1.60 ± 0.02	1.267 ± 0.011
$(-1, 3, 0.5)_{xy1}$	10.20 ± 0.04	$(6.19 \pm 0.02) \times 10^{-2}$
$(-1, 3, 0.5)_{xy2}$	-0.482 ± 0.007	1.64 ± 0.02
$(-1, 3, 0.5)_{xz1}$	10.3 ± 0.03	$(6.16 \pm 0.02) \times 10^{-2}$
$(-1, 3, 0.5)_{xz2}$	-0.480 ± 0.007	1.66 ± 0.02
$(-1, 3, 0.5)_{yy1}$	22.4 ± 0.6	$(5.75 \pm 0.02) \times 10^{-2}$
$(-1, 3, 0.5)_{yy2}$	1.47 ± 0.02	1.33 ± 0.02
$(-1, 3, 0.5)_{yz1}$	2.95 ± 0.07	$(5.11 \pm 0.07) \times 10^{-2}$
$(-1, 3, 0.5)_{yz2}$	-0.278 ± 0.002	0.989 ± 0.018
$(-1, 3, 0.5)_{zz1}$	6.63 ± 0.02	$(5.48 \pm 0.07) \times 10^{-2}$
$(-1, 3, 0.5)_{zz2}$	2.28 ± 0.02	1.390 ± 0.009

Table A.6: Parameters for all Maxwellian curve fits for current nulls.

$\mu\nu$	$a_{\mu\nu}$	$b_{\mu\nu}$	$\omega_{0\mu\nu}$
xx	3.34 ± 0.07	$(6.75 \pm 0.07) \times 10^{-2}$	$(-4.84 \pm 0.06) \times 10^{-2}$
xy	3.24 ± 0.05	$(6.27 \pm 0.04) \times 10^{-2}$	$(-4.33 \pm 0.05) \times 10^{-2}$
yy	3.30 ± 0.02	$(6.28 \pm 0.03) \times 10^{-2}$	$(-4.35 \pm 0.05) \times 10^{-2}$

Table A.7: Parameters for the translated Maxwellian curve for current null with parameters $(-1, 2, 3)$.

$(p, j_\parallel, j_\perp)_{\mu\nu}$	$\overline{v_\mu v_\nu}$
$(0, 0, 0)_{yy}$	$(9.87 \pm 0.06) \times 10^{-6}$
$(0, 0, -1)_{yy}$	$(6.10 \pm 0.09) \times 10^{-6}$
$(-1, 2, 0)_{xx}$	$(1.24 \pm 0.05) \times 10^{-3}$
$(-1, 2, 0)_{xy}$	$(1.24 \pm 0.05) \times 10^{-3}$
$(-1, 2, 0)_{xz}$	$(-3.42 \pm 6.16) \times 10^{-6}$
$(-1, 2, 0)_{yy}$	$(1.24 \pm 0.05) \times 10^{-3}$
$(-1, 2, 0)_{zz}$	$(0.77 \pm 3.03) \times 10^{-6}$
$(-1, 2, 3)_{zz}$	$(5.42 \pm 0.13) \times 10^{-4}$
$(-1, 3, 0)_{zz}$	$(1, 19 \pm 0.06) \times 10^{-4}$
$(-1, 3, 0.5)_{zz}$	$(9.77 \pm 0.18) \times 10^{-5}$

Table A.8: Tabulated values of the average squared velocities which define the delta functions for three-dimensional null cases.